The Pennsylvania State University

The Graduate School

Department of Electrical Engineering

# RF REFRACTION ON ATMOSPHERIC PATHS FROM RAMAN LIDAR

A Thesis in

Electrical Engineering

by

Paul Jason Collier

Submitted in Partial Fulfillment
of the Requirements
for the Degree of

Master of Science

August 2004

I grant The Pennsylvania State University the nonexclusive right to use this work for the University's own purposes and to make single copies of the work available to the public on a not-for-profit basis if copies are not otherwise available.

_____

Paul Jason Collier

We approve the thesis of Paul Jason Collier.

Date of Signature

| | |
|---|---|
| _____ | _____ |
| C. Russell Philbrick<br>Professor of Electrical Engineering<br>Thesis Adviser | |
| _____ | _____ |
| Victor Pasko<br>Associate Professor of Electrical Engineering | |
| _____ | _____ |
| Kenneth Jenkins<br>Professor of Electrical Engineering<br>Head of the Department of Electrical Engineering | |

# ABSTRACT

By combining three measurements of atmospheric properties, profiles of RF refractivity can be calculated, and the refraction of an electromagnetic wave caused by molecular scattering is determined. Raman lidar has been demonstrated to provide measurements of temperature and water vapor content in the lower troposphere. Using a ground-based pressure sensor, and applying the hydrostatic equation allows an accurate profile of pressure to be obtained through the lower atmospheric region. The PSU LAPS (Lidar Atmospheric Profile Sensor) system is able to provide this important parameter with continuous real-time profiles. A method is suggested which improves the detail seen in visual inspection by forming a ratio of the measured refractivity to values calculated from the U.S. Standard Atmosphere. The variations in refraction cause significant bending of the path of electromagnetic waves. The possible propagation paths result in the phenomena referred to as subrefraction and super-refraction. Ducting is an extreme case in which refraction of an electromagnetic wave causes the wave to bend to such a degree that it behaves as if in a waveguide along the surface of the Earth. This process causes radiation to travel much further along the Earth's surface than expected and greatly distorts the information in the backscatter signals. Modeling this refractive behavior is accomplished using the RPO (Radio Physical Optics) program. Two separate measurement campaigns are analyzed, one from the southeast coastal United States, and one from the Persian Gulf region. In the first campaign, examples are shown in which the LAPS system was able to measure minor ducting events in the lower troposphere. In the data sets from the Persian Gulf, major ducting events are described based upon

weather model data from four separate locations. Because the results demonstrate that refractive conditions happen on a regional scale, an argument is made that a relatively small number of lidar systems, deployed on ships in a coastal region, would provide a reliable picture of refractivity in a region.

# TABLE OF CONTENTS

## LIST OF FIGURES

# LIST OF TABLES

## ACKNOWLEDGMENTS

I would first like to thank my advisor, Dr. C.R. Philbrick, for his consistent encouragement and efforts to enrich my education. His guidance has been invaluable during my entire research experience. I would also like to thank Tom Petach, Bill Ryan, and Dr. Richard Clark for their support and advice, and I thank Steve Fast for his time and effort in assisting in the development of this thesis.

My colleagues, Sachin Verghese, Adam Willitsford, Sameer Unni, and Homer Li are due many thanks, as they have become more than just co-workers. The friendship that we have shared has encouraged me and helped to make the journey enjoyable, as well as educational.

The support that my family and friends have shown has been overwhelming. In particular, I thank my parents, Gary and Teresa Collier, for their enduring love and support.

I acknowledge the Navy sponsors, SPAWAR PMW 185, who provided support for the GRA through the PSU Applied Research Lab (ARL). Acknowledgements also go to the United States Environmental Protection Agency, grant # R826373, and to the Pennsylvania Department of Environmental Protection, contract ME#359494, for their support of my graduate research.

# CHAPTER 1

# INTRODUCTION

## 1.1 Thesis Objectives

When transmitting an electromagnetic wave, it is expected that the nominal propagation direction is a straight line from the antenna field calculated. In radiowave and radar applications, knowing where the signal is traveling is quite important. Yet the scattering phenomenon can change this path significantly, as happens in the case of ducting. The phenomenon of ducting occurs when small changes in the index of refraction of the atmosphere cause a wave-guide effect on radio frequency waves. The scattering by molecules in the atmosphere results in the refractive bending of the wave propagation direction. This effect can cause RF waves to travel along the surface of the Earth, hundreds of kilometers away from their sources.

Variations in the index of refraction, and therefore RF refractivity, depend upon scattering processes. Refraction depends upon gradients in atmospheric density, which is governed by temperature and pressure, and corresponds to the same phenomenon as optical mirages. The Pennsylvania State University Lidar Atmospheric Profile Sensor (LAPS) has the ability to measure specific humidity, temperature, ozone, and optical extinction using Raman scattering techniques, and these properties include the information on refraction. High-energy laser pulses are transmitted vertically, and the Raman shifted return signals are detected at the surface. At frequencies of less than 50 GHz, in the range of wavelengths corresponding to the microwave and radio wave spectrum, the specific humidity becomes the most important contributor to refraction.

Water vapor is important because it has a large electric dipole moment, and the gradients occurring in water vapor near the surface are quite large. Since LAPS has the ability to measure specific humidity and temperature directly, only the pressure profile needs to be calculated. This is done by measuring the pressure at the surface and using the hydrostatic equation to calculate the entire profile, which is a very close approximation to the actual profile and exhibits only small variations in the vicinity of strong vertical motion, such as regions of intense convection as occurs near cumulus clouds.

Ducting occurs when RF refractivity (measured in N-units, which are defined in Section 3.1) "decreases with altitude at a rate greater than about –157N per 1000 meters" [Helvey, 1994]. One objective of this thesis is to demonstrate that measurements taken by the Penn State University LAPS instrument are able to measure the RF refraction properties to provide proper description of the propagation of electromagnetic waves. In addition, data from the strong ducting conditions in the Gulf region (weather model data provided by Dr. Steve Fast of Remcom, Inc.) have been used to further understand the conditions under which ducting occurs.

This thesis will introduce a new and instructive method to examine refractivity profiles through visual inspection that is based upon variations from the United States Standard Atmosphere. Descriptions of the refractive effects will take advantage of a radio propagation model called Radio Physical Optics (RPO). Finally, this thesis will argue the point that operating a small number of lidar systems on Navy ships in a particular region could provide a regional description of how radio waves will propagate. The results show that vertical profiles from a few locations, such as those that would be

obtained from ships with Raman lidars, could be used to determine the propagation characteristics for all of the electromagnetic propagation within a littoral area.

## 1.2 Historical Background

In order to understand why refractivity measurements are of interest, a survey of some of the related research has been done. Most of the important research topics have been described in a report, the AGARD (Advisory Group for Aerospace Research & Development) Conference Proceedings 567, Propagation Assessment in Coastal Environments.

### 1.2.1 Overview of Sensing Techniques and Problem Considerations

Modern sensors must be able to handle electromagnetic propagation in an inhomogeneous environment. Coastal regions are especially prone to having spatial and temporal variations in atmospheric structure that can cause sensors to react in unpredictable ways. Examples include holes in radar coverage, as well as the picking up of objects far beyond the normal radio horizon [Richter, 1995]. Figure 1.1 illustrates these possibilities in regards to the presence of a surface duct. In the left panel of Figure 1.1, when no surface duct exists, the best altitude for aircraft to remain undetected is near the ocean surface. In the panel on the right, which shows coverage in the case that a surface duct exists, detection at the surface will occur far beyond the normal radio horizon, yet flying right above the duct will allow radar invisibility.

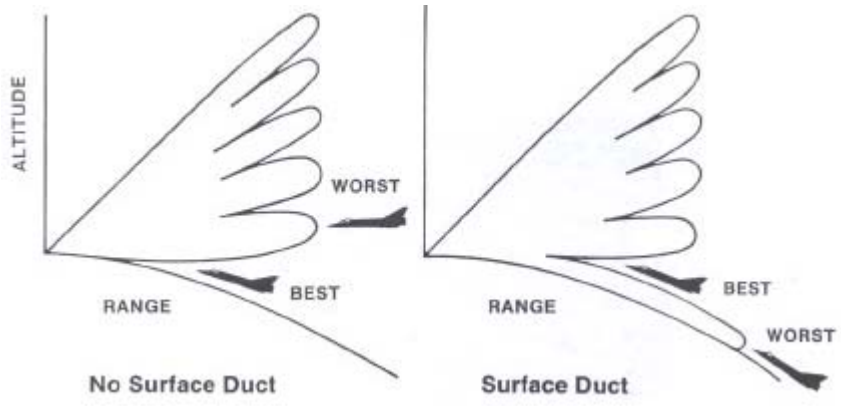


**Figure 1.1.** Tactical use of radar coverage [Wave Propagation Panel, 1990].

In the NATO report referenced above, Dr. Juergen H. Richter made a point that before addressing sensing techniques, it is important to establish *what* needs to be sensed, how *accurate* the measurements must be, and *where* they should be taken. From the long history of refraction research, we know that profiles of temperature, water vapor, and pressure are the required ingredients to evaluate refractivity. The primary factor of interest is the water vapor profile measurement, as its variability generally plays the biggest role in RF refractivity variations. Regarding accuracy of measurements, the most important consideration is the accuracy of vertical refractive gradients and their height. A resolution of 10-15 meters is sufficient to capture the significant gradients. Quickly noted is that although the Penn State University LAPS lidar system presented in this thesis has a resolution of 75 meters, it is still able to capture gradients with enough accuracy to provide useful results, and the proposed ALAPS (Advanced Lidar Atmospheric Profile Sensor) system will have a resolution of 15 meters [Philbrick, 2003, and Slick, 2002]. Finally, since horizontal homogeneity over the area of interest can be assumed, a single measurement is enough to characterize the refractivity in the immediate area around the sensor [Richter, 1995].

Many techniques have been used successfully to determine RF refractivity. The radiosonde is the most frequently used instrument, and it provides satisfactory vertical profiles of humidity, temperature, and pressure. Its shortcomings include non-continuous measurements (a vertical profile takes 30 minutes and rarely is a radiosonde launched more than once every few hours), local heat sources interfering with surface measurements, and a non-vertical sampling path (the balloon drifts horizontally with wind). Microwave refractometers measure RF refractivity directly at a point by use of a microwave cavity "whose resonant frequency is a function of both the dimensions of the cavity and the refractive index of the air" [Richter, 1995]. Although these instruments are considered to have the greatest degree of accuracy, as well as very rapid response times, they are very expensive and the point measurements are usually limited to measurements from helicopters. Radar techniques have been used for the purpose of studying refractivity since 1969, when Richter designed a radar just for that purpose [Richter, 1995]. Continuous measurements and good range resolution are advantages, while clouds and particulates can cause difficulties by contaminating the radar data. Also, because the radar measurements rely on turbulence-caused Doppler broadening, other effects that cause this broadening will cause contamination of data. Lidar techniques, including differential absorption lidars (DIAL) and Raman lidars, have proven to be successful in measuring temperature and water vapor concentrations. Daytime background radiation and aerosol extinction are limitations for lidar techniques; however measurements up to the cloud height and data through thin or patchy clouds have been demonstrated to provide fairly complete coverage during the LAPS tests at sea. The continuous, high-resolution vertical profiles are the big advantage of lidars. Details

on how a Raman lidar system works are given in Chapter 2. Another interesting set of techniques, referred to simply as "radio propagation techniques," involves monitoring of known radio transmitters. Coastal regions generally have an abundance of land-based transmitters, and these radio waves can be monitored passively offshore. In 1992, Hitney was able to derive correlations between radio signals and the height of the trapping layer (duct height) in the southern California coastal region. An alternative radio propagation technique involves monitoring of radio signals from satellites in order to relate refractive bending to refractive structure. An attempt at using GPS satellite signals by K.D. Anderson was somewhat successful, but not reliable enough to be recommended for routine use [Richter, 1995]. Finally, there is importance in detecting "evaporation ducts". An evaporation duct is caused by a rapid decrease in humidity right above the ocean surface [Richter, 1995]. In these cases, the water vapor profile rapidly decreases from saturation levels just centimeters above the surface. Detecting these ducts currently requires the measurement of four variables: sea-surface temperature, air temperature, relative humidity, and wind speed measured at a convenient reference height (usually about 5 - 10 meters). The conditions at the surface layer are then estimated using calculations that come from the Monin-Obukhov theory [Stull, 1997]. Typical instrumentation used for measurements of the surface duct include psychrometers, anemometers, and thermometers. For sea-surface temperature, a hand-held radiometer "may provide more convenient and accurate data" [Richter, 1995].

### 1.2.2 Overview of the Variability of Coastal Atmospheric Refractivity Program

A multi-year experiment to investigate the variability of atmospheric refractivity, with emphasis on the coastal zone, began with an intensive measurement period from 23 August to 3 September 1993. The motivation for this experiment began with the development of the Radio Physical Optics (RPO) program, and Hitney's use of it to demonstrate a capability to assess the height of the base of the trapping (duct) layer from observations of the radio signal strength. The VOCAR experiment was conducted jointly with the Naval Air Warfare Center Weapons Division, Point Magu, CA, the Naval Research Laboratory, and the Naval Postgraduate School. The National Oceanic and Atmospheric Environmental Laboratory and Penn State University/Applied Research Laboratory participated during the intensive measurement period mentioned above. The measurement campaign included data on radio wave propagation collected at two receiver sites and meteorological data collected from three profiler sites, eight radiosonde sites, three aircraft, and numerous surface weather sites [Paulus, 1995].

The VOCAR (Variability of Coastal Atmospheric Refractivity) experiment took place in the southern California coastal region. "Ducting is present in this area more than 70% of the time on an annual basis, the coastline geometry is well suited for propagation paths, and there are numerous transmitters already operating along the coast" [Paulus, 1995]. Automatic Terminal Information Service (ATIS) transmitters, which are located at many airports, provide convenient radio signals in the VHF/UHF band. Each transmitter has a partial overland path to one of two sites, either Point Magu near Oxnard, or Point Loma in San Diego. To ensure clear overwater paths, additional transmitters were installed on San Clemente Island. This is an excellent location, as the path length to

Point Magu (132 km) is nearly identical to the path length to Point Loma (127 km). Figure 1.2, adapted from [Paulus, 1995], provides a simple depiction of this situation, in which the angular separation of these two path lengths is 120 degrees. Differences in the signals over these two paths are able to "provide data on the inhomogeneity of the refractive structure," [Paulus, 1995].

During the intensive observation period conducted from Aug. 24 - Sept. 3, 1993, radio propagation conditions were measured at Point Magu and Point Loma with nearly identical receiver systems. The set of meteorological conditions provided the necessary inputs for the RPO program to arrive at a propagation prediction which was compared with the measured radio wave propagation Combining this with other propagation predictions from observed or forecast atmospheric structure, comparisons were made with the observed signals to validate the model predictions. The hope was to provide insight into such questions as: the required temporal and spatial resolution of meteorological data needed to characterize propagation conditions, and the capabilities of different types of sensors to provide such resolution. Some results suggested that subsidence-induced surface-based ducts tend to be homogeneous in range, while Santa Ana induced ducts tend to be inhomogeneous in range [Paulus, 1995].

The PSU LAMP lidar instrument was also used during the intensive observation period mentioned above. Five days of measurements were taken, and two frequencies were analyzed in RPO for each day to evaluate the qualitative aspects of the changing refractive effects and the propagation loss characteristics that would have been predicted, given the lidar profile data as input. The LAMP lidar measures temperature and water vapor mixing ratio in much the same fashion as is described for the LAPS instrument in

Section 2.4, and the refractivity values calculated for the VOCAR experiment were obtained using Equation 3.2, which required a surface pressure sensor and the use of the hydrostatic equation. Lidar refractivity profiles were calculated during the experiment, and RPO models were run to determine propagation loss from the given profiles. The data set shows that the lidar atmospheric sensor has proven to provide good temporal and vertical sampling of refractive variability. Conclusions have also shown that propagation predictions based on a single lidar profile are useful to provide "first order estimates of the losses that can occur on a propagation path" [Philbrick, 1995].

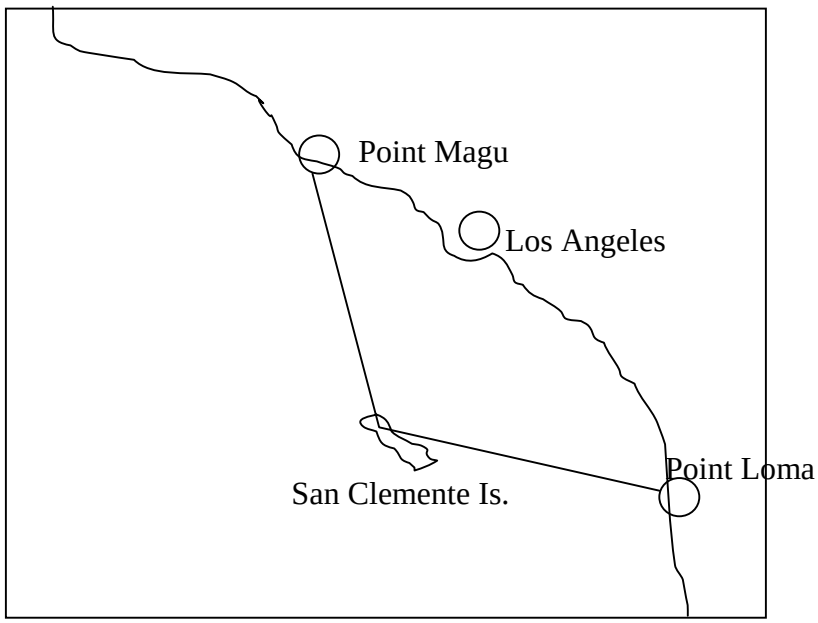


**Figure 1.2.** Map showing overwater paths of radio transmission [after Paulus, 1995].

### 1.2.3 Case Study of Coastal Remote Measurement of Atmospheric Refraction

Davidson and Walsh, of the Naval Postgraduate School (NPS), conducted studies evaluating the refractive conditions in the Norwegian and California coastal regions in 1991 and 1992 [Davidson, 1995]. Specifically, the research involved comparing airborne and ground-based measurements of the marine atmospheric boundary layer (MABL) with coastal in situ refractive measurements. The instruments involved in the study included the advanced very high resolution radiometer (AVHRR) satellite, airborne and ship based scatterometers, airborne and satellite based C-band synthetic aperture radars (SARs), and the Ground Based High Resolution Interferometer Sounder (GB-HIS).

The GB-HIS is an instrument that measures atmospheric radiance in the infrared spectrum, from 3.3 to 18.2 micrometers, with very high resolution. These measurements are used to derive near-continuous temperature and water vapor profiles for the lower troposphere [Davidson, 1995]. The sites from which data was gathered include two research vessel cruises by the R/V Point Sur off the central California coast on 8-10 May 1991, and 8-11 May 1992, as well as a coastal site at the Naval Air Station at Point Magu, California, during the Variation of Coastal Atmospheric Refractivity (VOCAR) experiment in August and September 1993. Radiosonde data was gathered to validate the GB-HIS data and to better understand the coastal environment. Generally the GB-HIS instrument did a good job at measuring the thermal structure of the MABL, but had a stark inability to "resolve the observed detailed moisture structure of the coastal boundary layer." Because of this weakness, the GB-HIS cannot be considered a reliable instrument to use for the purpose of refractive variation measurements [Davidson, 1995].

Satellite-based sensors launched in 1991 by the European Space Agency included the ERS-1 C-band scatterometer and synthetic aperture radar (SAR). The NPS had the task of examining the capability of these sensors to characterize high spatial variation in refractive conditions. The ERS-1 passed over the experiment site every 3 days. Meanwhile, in situ atmospheric and surface data were collected by researchers from the University of Bergen onboard the R/V Haakon Mosby (HM). Wind, temperature, and humidity were measured continuously from the HM, and radiosondes were launched with every pass of the satellite. This insitu data was obtained during the NORwegian Continental Shelf Experiment in November 1991 (NORCSEX'91). The findings concluded that the ERS-1 SAR was able to detect evaporation duct variations because the duct thickness was correlated with wind speed. Duct thickness changes are important to operational radars because the minimum frequency that would be significantly affected increased from near 10 GHz to above 100 GHz when the duct thickness decreased from 10 to 2 meters [Davidson, 1995]. The conclusion in this research was that the combination of the satellite data with that of the ship-based and airborne data was able to provide good estimates of the probability of the occurrence and nature of the significant refractive conditions [Davidson, 1995].

### 1.2.4 Resolution Requirements for Propagation Assessment

Determination of what horizontal separation between atmospheric profiles is adequate for shipboard assessment of propagation, as well as determination of the acceptable vertical resolution for accurate propagation assessment, is of fundamental importance. G. Daniel Dockery and Julius Goldhirsh, of the Applied Physics Laboratory

at Johns Hopkins University, examined two sets of high-resolution atmospheric data in order to attempt to answer these questions, one from the west coast, and one from the east [Dockery, 1995].

The JHU/APL has collected thousands of atmospheric profiles since 1984. Most of these profiles have been obtained through the use of a civilian helicopter equipped with pressure, temperature, and humidity sensors. Additionally, a dual-antenna radar altimeter was used to measure altitude accurately. These data were then analyzed using a two-step process. First an algorithm called LARRI (Large-scale Atmospheric Refractivity Range Interpolator) was used to filter out small fluctuations and to construct a physically reasonable range-interpolation between adjacent refractivity profiles. The steps LARRI performs are as follows [Dockery, 1995]:

1. Smoothes the individual refractivity files.
2. Extrapolates to the surface and to a user-specified height if necessary.
3. Fits line segments to the smoothed profiles.
4. Identifies and categorizes profile structures.
5. Finds best possible match of refractivity structures between adjacent profiles
6. Interpolates between profiles while preserving matched structures.

A propagation model called TEMPER (Tropospheric Electromagnetic Parabolic Equation Routine) was then used, which is based on the Fourier split-step numerical solution of the parabolic wave equation [Dockery, 1995]. A similar basis exists for RPO and is addressed in Chapter 3. LARRI and TEMPER produced averaged outputs over a box of approximately 2 km in range and 15 meters in height. The results in this study were

mainly focused on altitudes below 150 meters, because that is where refractive effects on propagation are most severe.

Results from San Nicolas Island off the coast of Southern California on March 19, 1988, and off the coast of Norfolk, Virginia were presented. Vertical resolutions of 6, 18, and 30 meters were tested in both places. Horizontal resolution of 8.5, 17, 25, and 59 km were analyzed. The two frequencies chosen as inputs into the models were 10 GHz and 3 GHz. In order to investigate the effects of degrading measurement quality, vertical propagation factor slices were examined at ranges of 30 km and 50 km away from the transmitter, while horizontal slices at heights of 30 m and 100 m were examined.

Many graphs are shown in the Dockery report, and visual inspection of the output graphs from the above-mentioned models was used to determine acceptable vertical and horizontal resolutions for propagation assessment. To summarize San Nicolas Island's results, 18 meter vertical resolution was the minimum to arrive at meaningful results, but 6 meter resolution was preferred. Using a horizontal resolution of less than 17 km resulted in a big drop in reliable observations. In the east coast case of Norfolk, VA, it was suggested that a 10 meter vertical resolution be the minimum to achieve acceptable results, while once again, a 17 km lateral resolution was desirable. The 3 GHz radar results showed significantly less sensitivity to a decrease in resolution than did the 10 GHz radar, as was expected. The resolution and frequency parameters given in these two cases assumed a propagation prediction accuracy of 5 dB. “If it was only necessary to predict propagating signal levels to within 15 dB, the resolution could be relaxed considerably” [Dockery, 1995].

### 1.2.5 Refractivity Profiles Inferred from GPS Signals

Tropospheric refractivity profiles are conventionally arrived at through the use of radiosondes, which are expensive and frequently undersample the spatial and temporal variability of weather phenomena. Anderson has presented research on a technique to "infer the vertical refractive profile of the lower atmosphere from ground-based measurements of GPS satellite signals as the satellite rises or sets on the horizon," [Anderson, 1995]. Four advantages of this technique have been noted. First, the inferred profiles will be representative of the integrated refractive effects along the range-height path instead of single point vertical profiles. Second, there are as many as 84 per day times when a GPS satellite will rise or set on the horizon. This means an adequate number of data profiles would be available to provide a picture of refractivity in an area. A receiver located near the equator will see rise and set locations nearly uniformly distributed in azimuth. Thirdly, this technique takes advantage of a multi-billion dollar system that is fully functional. And finally, the concept can be easily automated since, ideally, all that is required is a GPS receiver and a small computer for processing [Anderson, 1995].

Crucial to success of inferring the refractivity is detection and tracking of GPS signals when the satellite is near the horizon. For this reason, the task of selecting a GPS receiver proved to be challenging for Anderson's group, as most commercially available receivers are designed to respond well when the satellite is well above the horizon. Three manufacturers had receivers that could be usable, including Allen Osborne Associates, Ashtech, and Trimble Navigation. Testing of the three receivers ensued, and the

researchers chose the Turbo Rouge from Allen Osborne Associates, as it was the "best" choice, even though it was not ideal.

GPS satellite signal measurements were made on six days in June and July of 1994. Surface and upper air meteorological measurements were made near the receiver site, and an instrumented aircraft was flown at about 30 meters above the ocean surface to measure air temperature, dew point temperature, sea surface temperature, atmospheric pressure, and altitude [Anderson, 1995]. At designated points, the aircraft ascended in a spiral to an altitude of about 500 meters, and then descended to the original altitude, so that a separate source of vertical profiles could be determined.

Initial results taken on July 28, 1994, showed that refractivity profiles measured by both a balloon-launched radiosonde, and the aircraft, indicated an elevated duct. Propagation loss was calculated using a ground-to-satellite modified version of RPO. With higher elevation angles (smaller subsatellite range), RPO showed good agreement with the ground-based loss measurements of the satellite signal. However, with elevation angles less than about 2 degrees, where the shape of the refractivity profile has the greatest influence, substantial difference exists between the model and the measurements. No general conclusions could be made, but results of the GPS technique were "very encouraging," [Anderson, 1995].

A more recent study was conducted by Lowry, et al, in which experiments were conducted off the coast of San Diego, California, from October 1999 to April 2000, to estimate refractivity using ray propagation models to fit measured GPS tropospheric delays in a least squares metric. These estimates of refractivity structure were compared with nearby radiosonde measurements.

The observable that was used in these experiments to constrain refractivity was the excess phase path, which can be described as the excess travel time between satellite and receiver that results from tropospheric bending and slowing, multiplied by the speed of light in vacuum [Lowry, et al, 2002]. The GPS excess phase path was estimated using a modified version of Bernese v4.2 software [Lowry, et al, 2002]. Information retained after Bernese processing included the position of the receiver (which was fixed), the position and velocity of the GPS satellite derived from the precise ephemerides, and the measured excess phase path, $\Delta S^{GPS}$.

An example of the measured excess phase path is shown in Figure 1.3. The $\Delta S^{GPS}$ varied from about 2 meters at zenith to more than 100 meters at low satellite elevation angles. Lowest elevation data were prone to gaps in observations partly because of masking by structures and topography east of the instrument and partly because of multipath cancellation. Lowry noted that most of the information about the vertical distribution of refractivity is contained at low satellite elevation angles less than about 5 degrees, and of the 70 processed satellite rises and sets depicted in Figure 1.3, only 27 had usable observations at those elevations. On average the research group collected 24 usable rises and sets per day over the course of the experiment [Lowry, et al, 2002].

In order to parameterize the GPS measurement of excess phase path, $\Delta S^{GPS}$, an array of refractivity models, $N(r) = 10^6 \times [n(r) - 1]$, was assumed and compared to the measured excess phase path to determine which model provides the best fit in a least squares sense. The model design was motivated by a desire to characterize anomalous refractivity gradients. In comparisons with radiosondes launched from Point Loma, where the receiver was located, generally the model refractivity profiles arrived at from

$\Delta S^{GPS}$ fit the radiosonde profiles very accurately. In fact, 3 out of 4 of the models mentioned in Lowry's paper that come from $\Delta S^{GPS}$ fit the radiosonde profiles nearly

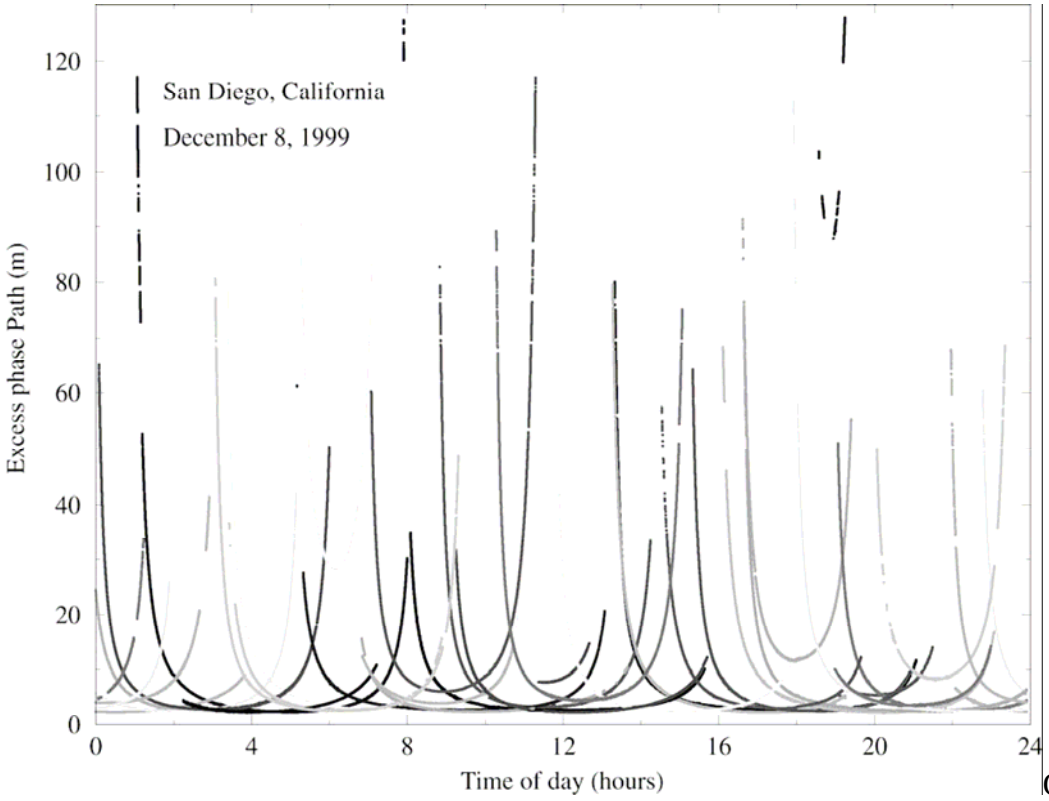


**Figure 1.3.** Measured excess phase path $\Delta S^{GPS}$ as a function of time on December 8, 1999 [Lowry, et al, 2002].

perfectly. In one case, the radiosonde profile only matched up moderately well, but overall a good correlation was seen at Point Loma between model predictions and radiosonde measurements.

Radiosonde measurements from Miramar, a location approximately 20 km from the Point Loma site, did not prove to be as successful in demonstrating correlation between refractivity models predicted from GPS measurements of excess phase path and profiles from the radiosondes themselves. This was attributed mostly to spatial inhomogeneity, and so conclusions in this experiment had much to do with minimizing spatial and temporal separation between GPS and in situ measurements. If this goal is

met, then refractivity estimated from $\Delta S^{GPS}$ is able to predict nearby radiosonde refractivity better than an average or reference model (e.g., CIRA + Q). This was shown well with the Point Loma radiosonde data [Lowry, et al, 2002].

### 1.3 Concluding Remarks

Instruments and techniques for measuring refractivity profiles have been around for at least 50 years. The studies presented here demonstrate the ability to make measurements that will allow acceptable prediction of radio wave propagation. All of the researchers agree that of utmost importance is understanding spatial and temporal variation of tropospheric refractivity, yet a complete solution has not been fully developed. Each technique examined presented its own advantages and disadvantages. It is hoped that this thesis will provide a useful solution for furthering measurements of regional refractivity variations.

# CHAPTER 2

# INSTRUMENTATION AND MEASUREMENT TECHNIQUES

## 2.1 Introduction to the Lidar Atmospheric Profile Sensor (LAPS) Lidar

The Penn State LAPS instrument is a monostatic Raman lidar system, which was developed as an operational prototype for the US Navy in 1996. The original purpose of LAPS was to demonstrate that a multi-wavelength Raman lidar would be able to make measurement profiles of RF refractivity and meteorological properties aboard Navy ships. Since then, it has been used to make meteorological measurements and to assist in studies of air pollution. The instrument has the ability to examine a wide range of meteorological conditions, by taking simultaneous measurement profiles of water vapor, ozone, temperature, and optical extinction.

## 2.2 Components of the LAPS Lidar

The Penn State LAPS lidar is made up of several subsystems, which include the transmitter, receiver, control system, detector, data collection electronics, and display monitor. The transmitter, receiver, and control system are housed together in a weather-tight unit, allowing the system to be used during most weather conditions. Additionally, this “deck unit” includes an air conditioner and heater to control the operating environment. On the top of the deck unit, a radar with a 6-degree conical angle detects approaching aircraft. On detection, a signal is sent to interrupt the laser Q-switch, which prevents possible eye-endangering radiation levels from direct view or specular

reflection. The control console contains the detector, data collection electronics, and display monitor. This unit is separate and placed in-doors, where the operator can set the operating conditions and observe the real time data display. The deck unit and control console are connected through power lines and fiber optic cables. These allow the lidar to be controlled remotely and the signal from the telescope to be transferred to the detector. Table 2.1 defines the primary subsystems of LAPS.

**Table 2.1** Summary of LAPS subsystems.

| | | |
|---|---|---|
| Transmitter | Continuum 9030 –30 Hz<br>5X Beam Expander | 600 mJ @ 532 nm<br>130 mJ @ 266 nm |
| Receiver | 61 cm Diameter Telescope<br>Focal length – 1.5 m | Fiber optic transfer |
| Detector | Eight PMT channels<br>Photon Counting | 660 and 607 nm – Water Vapor<br>528 and 530 nm – Temperature<br>295 and 284 nm – Daytime Water Vapor<br>277 and 284 nm – Raman/DIAL Ozone<br>607, 530, and 284 nm – Extinction<br>532 nm – Backscatter |
| Data System | DSP 100 MHz | 75-meter range bins |
| Safety Radar | Marine R-70 X-Band | Protects 6° cone angle around beam |

The LAPS transmitter is a Nd:YAG laser with a fundamental wavelength of 1064 nm. The laser is pulsed at 30 Hz and has a maximum output power of 1.6 joules per pulse. This total power results from the combined effects of a single laser oscillator and two power amplifiers. A pair of frequency doubling crystals follows the second amplifier, producing output wavelengths of 532 nm and 266 nm. The measurements taken do not require transmission of the fundamental wavelength, so the 1064 nm light is reflected onto a water-cooled beam dump, via a dichroic beamsplitter. The visible and UV wavelengths continue through the system into a 5X beam expander. This brings the

diameter of the beam at the $1/e^2$ points from .9 mm to 4.5 cm. This larger cross section lowers the power density to within ANSI standards for diffuse reflection observations beyond the near-field, while reducing beam divergence to allow a smaller field of view for the receiver, thus effectively reducing the contribution of background sky radiance. The LAPS transmitter characteristics are summarized in Table 2.2, while the transmitter optics are shown in Figure 2.1.

**Table 2.2** LAPS transmitter characteristics.

| | |
|---|---|
| Laser | Continuum Model 9030 with 5X Beam Expander |
| Pulse Repetition Frequency | 30 Hz |
| Pulse Duration | 8 ns |
| Fundamental Power | 1.6 J/Pulse |
| Power Output at 1064 nm | Dumped into heat sink |
| Power Output at 532 nm | 600 mJ |
| Power Output at 266 nm | 120 mJ |

The receiver consists of a parabolic mirror and a fiber optic cable located at the prime focus of the mirror. The mirror has a diameter of 61 cm and a focal length of 1.5 m. The fiber optic cable has a diameter of 1 mm, and it transfers the received signal to the detector box. The location of the face of the fiber cable is critical, so the position is adjusted using computer-controlled micropositioners. The receiver subsystem is shown in Figure 2.2.

Following the capture of the scattered radiation in fiber optic cable, the signal travels through the cable to the detector box. The diverging beam from the fiber is collimated using a 38-mm focal length plano-convex lens. A dichroic beam splitter, positioned at 45 degrees relative to the beam, then separates the UV wavelengths, while allowing the visible wavelengths to pass through. Seven narrow band-pass filters are

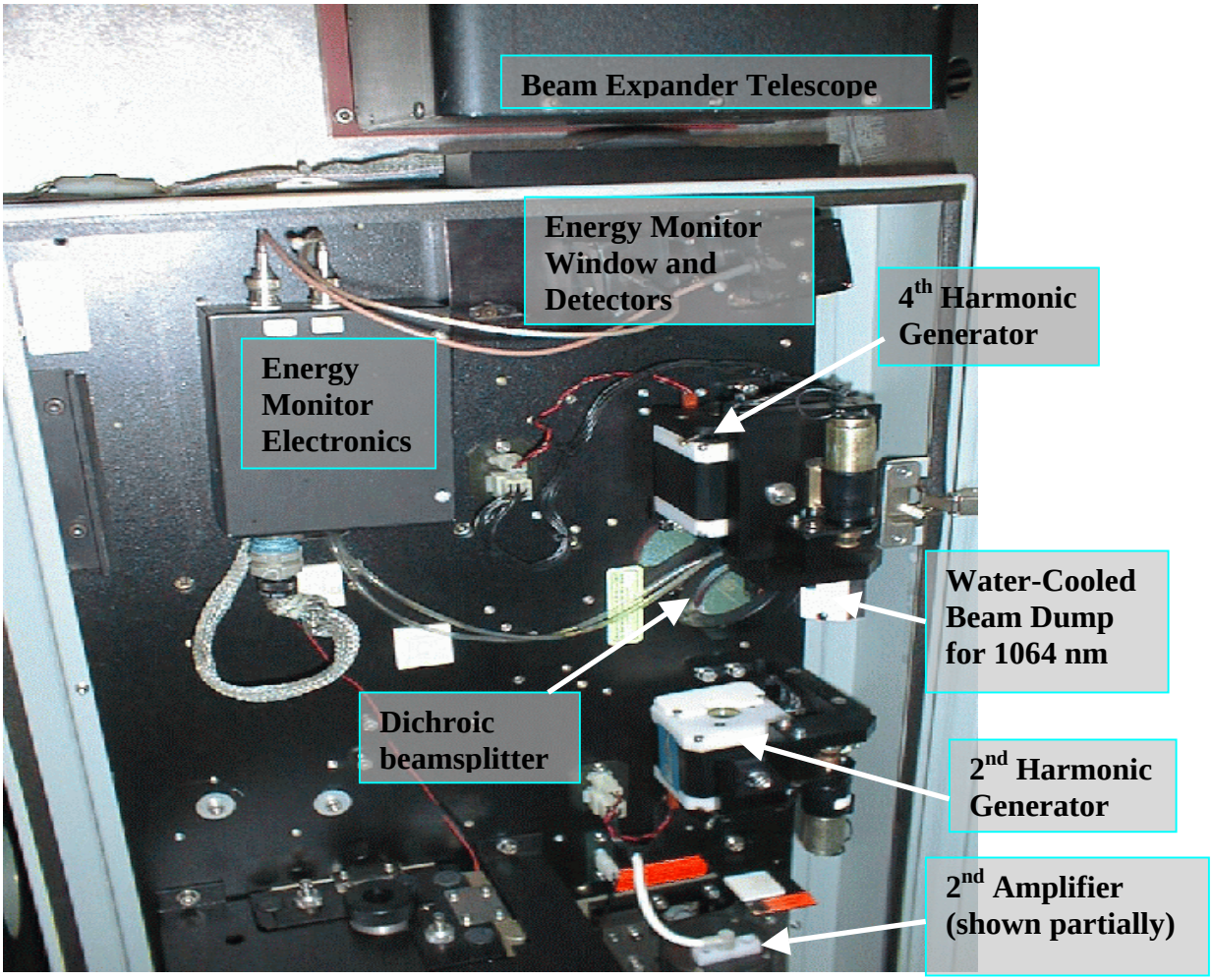


**Figure 2.1.** LAPS Transmitter optics (photo credit, C.R. Philbrick).

used to separate the signals into the specific wavelengths that correspond to the Raman return signals. Additionally, an eighth narrow band-pass filter is used to allow the detection of the unshifted 532 nm backscatter signal.

After passing through the filters, each signal enters a photomultiplier tube (PMT). Because Raman scattered signals are very low in intensity, the PMT's are operated in photon counting mode. This mode separates each photoelectron that is generated at the photocathode into a current pulse because it is multiplied by a large gain factor, and

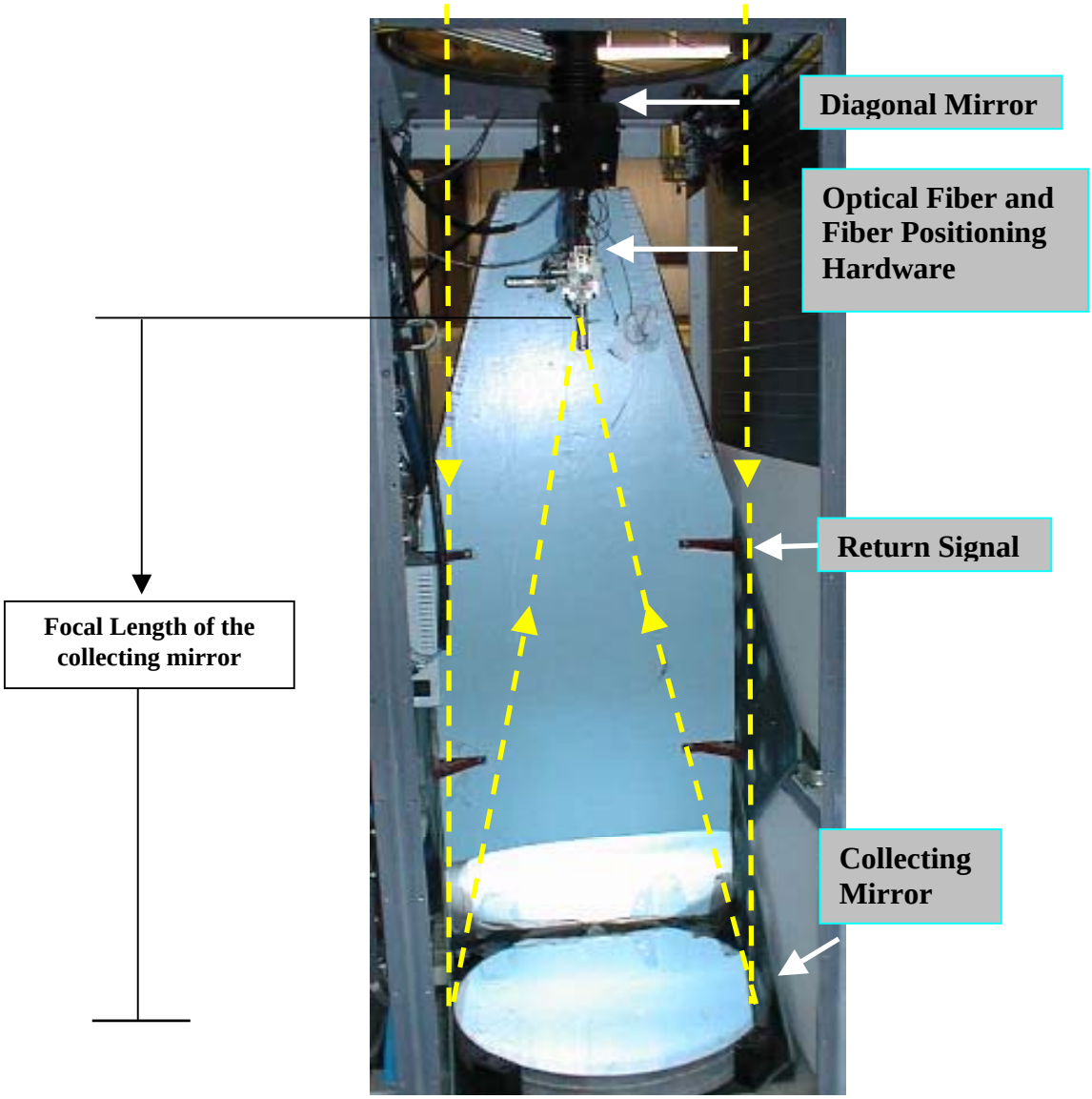


**Figure 2.2.** Receiver components and schematic of received beam (photo credit, C.R. Philbrick).

individual current pulses are counted when they exceed a set threshold. This approach was chosen to include gain stability, reduce dark current effects, and increase the dynamic range. The seven primary PMT's give a range resolution of 75 m, while the backscatter PMT uses a new higher speed detector and has a resolution of 3 m.

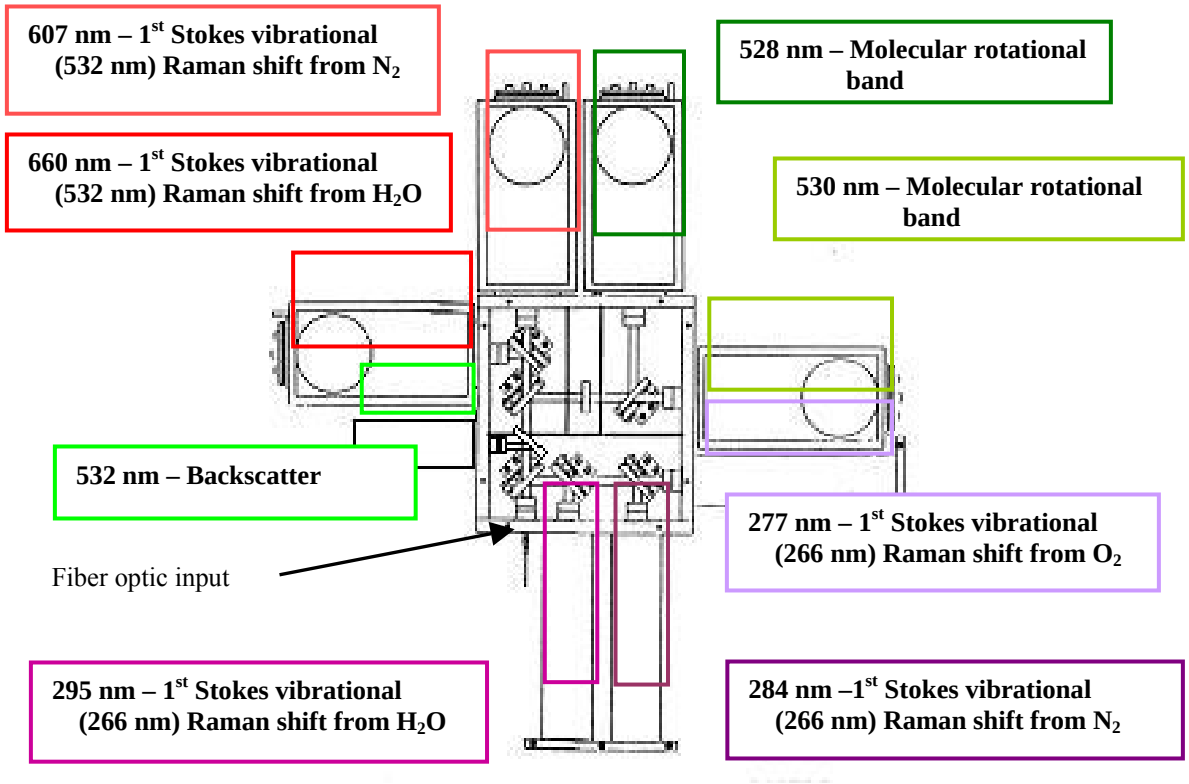


**Figure 2.3.** LAPS detector box with steering optics and PMT layout [Verghese, 2003].

A data acquisition system transfers the data from the PMT's (as raw photon counts) to raw data files. These files have the number of counts received in each range bin, which is assigned to a height, and the results are displayed on the console monitor in real-time. The console computer uses the lidar equation to process these raw data files, and displays provide results as real-time graphs of water vapor and temperature. New graphs appear every minute during operation, and the raw data files are saved for later processing and further analysis.

## 2.3 Principle of Raman Scattering

As mentioned previously, the LAPS lidar takes advantage of the principle of Raman scattering to make measurements. Raman scattering is inelastic, which means that the energy of the scattered photon is shifted significantly from the energy of the incident photon. This is different from the case of elastic scattering that is commonly referred to as Rayleight scattering. The term Rayleigh scattering really includes both the central (Cabannes) line and the nearby true rotational Raman lines. The frequency of the scattered photon in the Cabannes line matches that of the incident radiation, only differing by the frequency shift due to the wind Doppler velocity, and broadening due to the Doppler velocity from random thermal motion.

The energy difference in Raman scatter corresponds to the energy associated with the difference between the initial and final vibrational and rotational energy states of the molecule that scatters the photon. The Raman scatter frequency shifts are seperated into two classes, Stokes and anti-Stokes. Stokes is the more common type, and it occurs when the scattered photon loses energy to the molecule. This photon now has a lower frequency, and longer wavelength. In the anti-Stokes transition, the scattered photon will gain energy from the molecule. The vibrational transition, in which the photon ends up having a higher frequency or lower wavelength, is rare compared to the Stokes case because the simple atmospheric molecules rarely populate the vibrational states above the ground level at the normal range of temperatures. Figure 2.4 illustrates these molecular transitions. The case on the far left occurs most frequently, and shows that a photon striking a molecule at the ground vibrational level will cause the molecule to elevate to a

virtual energy level, followed by the scattering of a photon of equal energy to the incident photon, thereby returning the molecule to the ground state again. The middle (Stokes) case shows the much less frequent phenomenon in which the molecule returns to some elevated state above ground, thereby releasing a photon with an energy, ΔE, less than that of the incident photon. Finally, the least common occurrence (anti-Stokes) is shown in the righthand part of the diagram. This case shows a molecule existing in an elevated vibrational state being excited by a photon, which boosts it to a higher virtual energy level, and when returning to the ground state, it releases a photon with an energy, ΔE, higher than the incident photon.

## 2.4 The Lidar Equation

As stated earlier, photomultiplier tubes detect individual photons at a wavelength limited by the narrow band filters placed in front of each PMT. These photon counts can be interpreted as a power, $P(\lambda_R,z)$, in the scattering lidar equation given by Measures [1984] in Equation 2.4 below:

$$P(\lambda_R, z) = P_T(\lambda_T)\xi_T(\lambda_T)\xi_R(\lambda_R)\frac{c\tau}{2}\frac{A}{z^2}\beta(\lambda_T, \lambda_R)\exp\left[-\int_0^z[\alpha(\lambda_T, z') + \alpha(\lambda_R, z')]dz'\right] \qquad [2.1]$$

where,

| | |
|---|---|
| $z$ | is the altitude of the volume element from which the return signal is scattered [m], |
| $\lambda_T$ | is the wavelength of the laser light transmitted [m], |
| $\lambda_R$ | is the wavelength of the signal received [m], |
| $P_T(\lambda_T)$ | is the power transmitted at wavelength $\lambda_T$ [W], |

$\xi_T(\lambda_T)$ is the net optical efficiency at wavelength $\lambda_T$ of all transmitting elements [unitless],

$\xi_R(\lambda_R)$ is the net optical efficiency at wavelength $\lambda_R$ of all receiving elements [unitless],

$c$ is the speed of light in air [m $s^{-1}$],

$\tau$ is the bin duration [s],

$A$ is the area of the receiving telescope [$m^2$],

$\beta(\lambda_T,\lambda_R)$ is the backscatter cross section [$m^{-1}$] of the volume element for the laser wavelength $\lambda_T$ at Raman shifted wavelength $\lambda_R$ [$m^{-1}$],

$\alpha(\lambda,z')$ is the extinction coefficient at wavelength $\lambda$ at range $z'$ [$m^{-1}$].

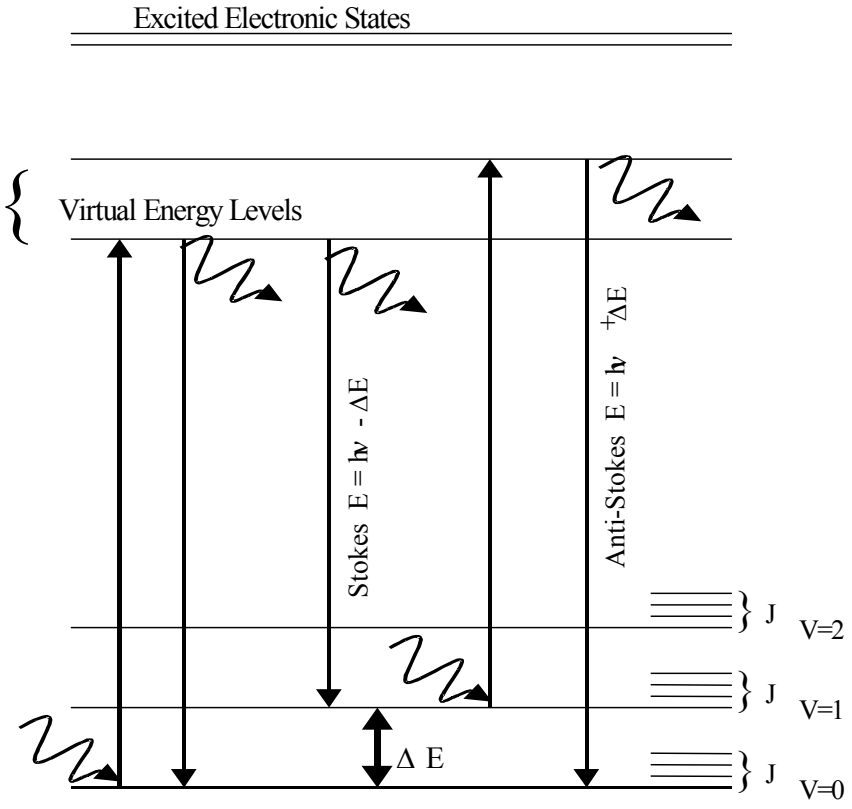


**Figure 2.4.** Energy diagram representation of the Stokes and anti-Stokes components due to Raman scattering [Philbrick, 1994].

The $c\tau/2$ component of this equation gives the bin size. With $\tau$ = 500 ns, the LAPS lidar system has a bin size, and thus a resolution of, 75 m. The rest of the components are known from the hardware component specifications and laboratory measurements, except for the extinction coefficient $\alpha(\lambda,z')$. Solving the equation therefore allows the signal profile to be calculated for a given Raman-shifted wavelength and range bin. This can be related to number density of a particular molecule in the atmosphere.

### 2.4.1 Water Vapor Measurement

The profiles of the two primary meteorological variables needed to calculate RF refractivity in the atmosphere are temperature and water vapor mixing ratio (specific humidity). LAPS has the ability to measure water vapor by taking the ratio of the 1st Stokes vibrational Raman shifts for water vapor and nitrogen. The equation used to determine water vapor profiles can be derived from taking the ratio of Eq. 2.1 written for $H_2O$ to the one for $N_2$ and yields:

$$W(z) = K_{cal}\frac{S_{H2O}(z)}{S_{N2}(z)} \quad , \qquad [2.2]$$

where,

$S_{H2O}$ is the received signal from the vibrational Raman shift of $H_2O$ at 660 nm (night-time), and at 295 nm (day-time),
$S_{N2}$ is the received signal from the vibrational Raman shift of $N_2$ at 607 nm (night-time), and at 284 nm (day-time)
$K_{cal}$ is a calibration constant.

The calibration constant, $K_{cal}$, can be determined by fitting the ratio of $S_{H2O}$ to $S_{N2}$ to radiosonde data, or it can be determined from the measured properties of the two data channels taken together with the scattering cross-sections. Although this ratio causes most of the terms in the lidar equation to drop out, a correction must be made for molecular scattering. This correction is applied because of the $1/\lambda^4$ dependence of the extinction coefficient on molecular scattering cross section. The wavelength dependence of aerosol scattering is small in comparison with that of molecular scattering, so it can be neglected in most cases. After this correction, Equation 2.2 becomes:

$$W(z) = K_{cal}\frac{S_{H2O}(z)}{S_{N2}(z)}\exp(\sigma_{H2O} - \sigma_{N2})G(z), \qquad [2.3]$$

where,

$\sigma_x$ is the is the Raman cross-section of x at the laser wavelength,
G(z) is the difference in molecular scattering.

The term G(z) is derived using the standard atmosphere and can be obtained using the following relations:

$$G(z) = \int_0^z NH(z)\left[1 - \exp\left(\frac{z'}{H(z)}\right)\right]dz', \qquad [2.4]$$

$$H(z) = \frac{kT(z)}{mg}, \qquad [2.5]$$

$$T(z) = T_0 + \gamma z, \qquad [2.6]$$

where,

N is the number density at ground level,
k is Boltzmann's constant,
m is average mass per mole,
g is gravitational acceleration,

$T_0$ is the surface temperature,
$\gamma$ is the lapse rate of –.0065 K/m.

A separate correction is needed when taking mixing ratio measurements with the ultraviolet at 266 nm. Mixing ratio measurements are obtained both day and night at this wavelength because the transmitted wavelength is in the "solar blind" region of the spectrum. This region from 230 nm to 300 nm is where stratospheric ozone absorbs much of the solar radiation. While this is a benefit in allowing the measurements to be made, it also means that the return signal needs to be corrected for ozone absorption in the lower troposphere. This correction is determined by taking the ratio of the vibrational Raman signals of $O_2$ to $N_2$ and using the fact that the $O_2/N_2$ ratio is constant in the lower atmosphere to calculate the extinction due to ozone. Therefore, the water vapor ratio at UV wavelengths is given by:

$$W(z) = K_{cal} * \frac{S_{H2O}(z)}{S_{N2}(z)} \left( \frac{S_{O2}(z)}{S_{N2}(z)} \right)^{\frac{\sigma_{H2O} - \sigma_{N2}}{\sigma_{N2} - \sigma_{O2}}}, \qquad [2.7]$$

where the differences in density and channel sensitivity are included in the $K_{cal}$ value, and $S_{O2}$ is the received signal from the vibrational Raman shift of $O_2$ at 277 nm [Mulik, 2000].

### 2.4.2 Temperature Measurement

Temperature is the second variable needed to derive RF refractivity because it governs the number density profile where hydrostatic equilibrium determines the pressure

profile. In the LAPS system, Raman lidar measurements of temperature depend on the rotational Raman wavelength-shifted return signals from $N_2$ and $O_2$. The signals are spectrally very close, and therefore the small difference in extinction between the two signals can be neglected [Haris, 1995]. Since the rotational spectrum changes with temperature, the ratio of the combined signals of $N_2$ and $O_2$ at 528 nm and 530 nm provide a temperature profile. Shown in Figure 2.5 are the ca Additionally, taking this ratio causes all of the system parameters except for filter functions to drop out. The ratio is described in the following equation [Balsiger et al, 1996]:

$$R(T) = \frac{\sum_S \sum_J N_S \times A_S(J,T) X f_{530,S}(J)}{\sum_S \sum_J N_S \times A_S(J,T) X f_{528,S}(J)} = \frac{C_{530}}{C_{528}}, \qquad [2.8]$$

where,

| | |
|---|---|
| $R(T)$ | is the lidar ratio as a function of temperature, |
| $S$ | is the summation index over the molecular species, |
| $J$ | is the summation index over the quantum numbers of the rotational states, |
| $N_S$ | is the fraction of the species in the atmosphere, |
| $A_S(J,T)$ | is the thermal population distribution of the rotational states, |
| $f_{530,S}$ | is the filter transmission function of the 530-nm channel, |
| $f_{528,S}$ | is the filter transmission function of the 528-nm channel |
| $C_x$ | is measured signal at $\lambda = x$. |

The temperature ratio has to be fitted to a radiosonde balloon for calibration. The fit is done using a least squares method, with the following equation:

$$T(R) = aR^2 + bR + c \quad , \qquad [2.9]$$

where,

| | |
|---|---|
| T(R) | is the temperature as a function of the lidar signal ratio, |
| R | is the lidar ratio of the 530-nm signal and the 528-nm signal, |
| a, b, and c | are calibration constants determined from filter sonde data. |

The calibration constants are initially determined by the sensitivities of the filters and then calculated by adjusting the fit to the radiosonde data.

### 2.4.3 Time Sequences from Raman Lidar

Using the methods described in Sections 2.4.1 and 2.4.2 to calculate temperature and water vapor, vertical profiles are obtained for each of these variables. Refractivity can be calculated from these profiles, and the method for this is shown in Section 3.1. However, visual representation of these two variables in the form of time sequences aid in describing meteorological events, and have been very useful in many campaigns. Examples of water vapor and temperature time sequence graphs from a 1999 LAPS campaign are shown in Figures 2.5 and 2.6. The graphs show a particularly hot and humid day, and structures such as surface heating and planetary boundary layer height can be seen rather clearly here. The ability to display data in this manner can contribute greatly to the understanding of lower tropospheric meteorology.

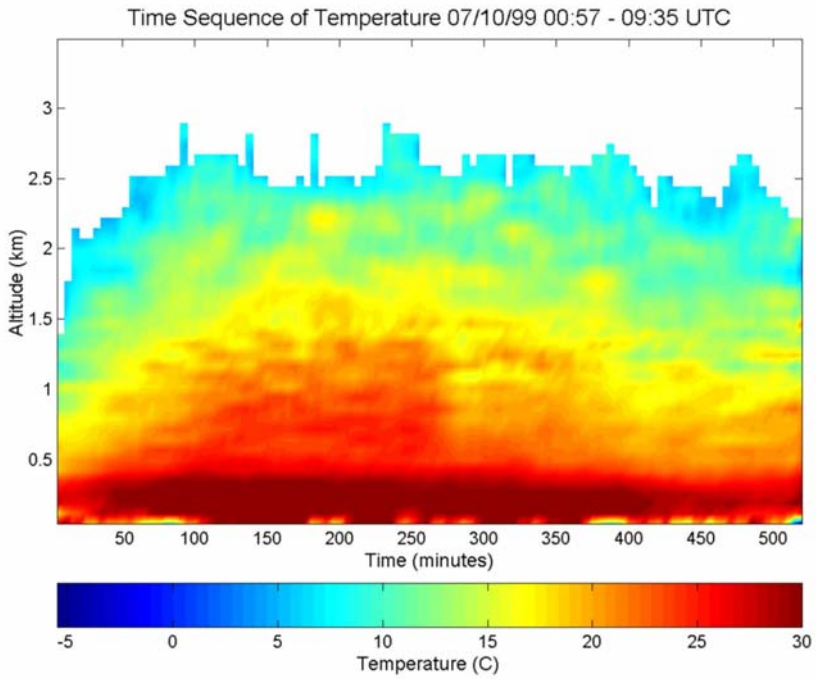


**Figure 2.5.** LAPS time sequence of temperature from 1999 campaign.

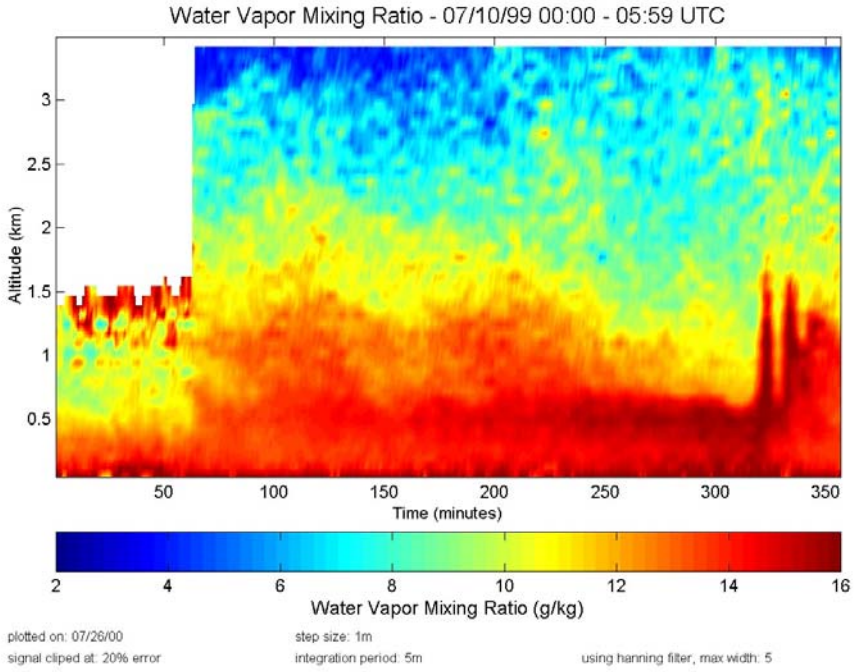


**Figure 2.6.** LAPS time sequence of water vapor from 1999 campaign.

# CHAPTER 3

# RF REFRACTION AND PROPAGATION CALCULATIONS

## 3.1 RF Refractivity

The spatial variance in the index of refraction at radio wavelengths in the atmosphere is what is known as RF refractivity. On the molecular level, picturing a distribution of scattering particles provides a good understanding of what causes refraction. As electromagnetic waves propagate through molecules and aerosols, they are scattered from individual particles. The idea described by Huygen's Principle helps to visualize the process in which the scattered wavelets from each particle combine to produce a final wavefront. Based on the constructive and destructive interference between the individual scattered wavelets, the direction of the combined wavefront can bend from it's incident direction. The temperature distribution has an effect on this phenomenon because particle density is directly related to temperature. Water vapor is very important in this process because of its large electric dipole moment and the strong gradients in water vapor distribution. As shown in Figure 3.1, the water molecule is asymmetric, and this causes a permanent dipole moment in the direction of the more positive hydrogen atoms. The relative strength of the dipole moment affects the scattered intensity. Because the electric dipole moment of the water molecule is large, even though the water molecule concentration is small, typically less than a perecent, its overall effect in the scattering process is quite significant.

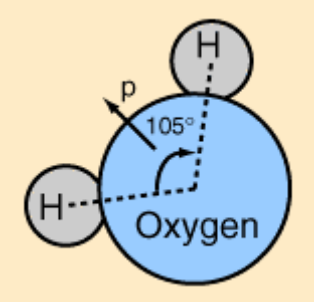


**Figure 3.1** Molecular structure of water, showing direction of dipole moment [Nave, 2003].

Measurements of the profile of index of refraction allow description of how radio frequency waves will bend when propagating. Because the index of refraction in air near the surface of the earth typically ranges between 1.00025 to 1.0004, refractivity is conveniently measured in N-units, given by:

$$N = (n - 1) * 10^6, \qquad [3.1]$$

From this equation, it follows that common values of refractivity fall in the range of 250 to 400 N-units. For radio/radar frequencies, refractivity can be determined from the following equation through measurements of pressure, temperature, and humidity [Helvey et al, 1994]:

$$N = 77.6\ P/T + 373000\ e/T^2, \qquad [3.2]$$

where,

P is the atmospheric pressure in millibars,

T is the temperature in degrees Kelvin,

e is the water vapor pressure in millibars.

The LAPS lidar instrument includes a ground pressure sensor to provide the base value during field campaigns. The hydrostatic equation can then be applied to calculate pressure at all altitudes in the range of interest:

$$\partial P = -\rho g \partial z\,, \qquad [3.3]$$

where,

$\partial P / \partial z$ is the derivative of pressure (P) with respect to height (z),

$\rho$ is the density of the air in kg/m$^3$,

g is the acceleration of gravity in m/s.

Integrating and using some substitutions, Equation 3.3 becomes:

$$P = P_0 \cdot e^{-z/H_0}\,, \qquad [3.4]$$

where,

$P_o$ is the surface pressure,

z is the alititude,

$H_o$ is the scale height, kT(z)/mg (see Eq. 2.5).

As pointed out earlier, the RF refractivity calculation depends upon the water vapor concentration at each altitude. The water vapor partial pressure is obtained from the mixing ratio and the atmospheric pressure as in the equation [Salby, 1996]:

$$e = \frac{rP}{r + 621.98}\,, \qquad [3.5]$$

where

r is the mixing ratio in g/kg,

621.98 is the ratio of specific gas constants from dry air and water.

The lidar measurements of specific humidity and temperature, and the surface pressure values can be entered into Equations 3.2, 3.4, and 3.5 to provide profiles of how the index of refraction changes in the atmosphere.

A useful parameter, known as modified refractivity, takes the Earth's curvature into account. This value is calculated from N-units and altitude (in meters) as shown below:

$$M = N + 0.157z. \quad [3.6]$$

This value is very useful, and it provides an immediate interpretation for long distance propagation. When M decreases with altitude, the phenomenon known as *ducting* occurs. As is explained briefly in Chapter 1, ducting is essentially the trapping of RF waves within a given height layer around the curvature of the Earth. This condition allows for the extended propagation of waves to distances much greater than normal. Ducts may be categorized as elevated, surface-based elevated, or surface. Idealized profiles of each of these conditions are shown in Figure 3.2. Figure 3.2(a) shows the "optimum coupling height", which is found in the ducting layer at the point where the relative maximum in M-unit values occurs. Energy is most effectively trapped at this altitude, compared with the rest of the ducting layer. The elevated duct seen in this figure would have almost no effect on near-surface radio/radar systems, but would be significant for aircraft or mountain top transmitters. In Figure 3.2(b), a surface-based duct is shown, and in this case, radar systems would be impacted substantially. Finally, Figure 3.2(c) shows a surface duct, in which the optimum coupling height is at ground level. This situation causes the largest amount of downward refractive bending, and therfore significant radar clutter will occur from the emitter outward to ranges well beyond the normal radio horizon. These surface ducting situations cause the most concern for surface radar applications, and are what need to be evaluated most carefully.

Alternative radar propagation situations include standard propagation, subrefraction, and super-refraction. Standard propagation results in expected radar propagation patterns. Subrefraction is the case in which a radio wave curves upward away from the Earth, and super-refraction occurs when a radio wave bends toward the surface but not enough to overcome the Earth's curvature and cause ducting. The four possible radio-wave propagation behaviors are shown in Figure 3.3. Although all of these conditions are important to understand, ducting cases are the most extreme and cause the most unexpected propagation behavior.

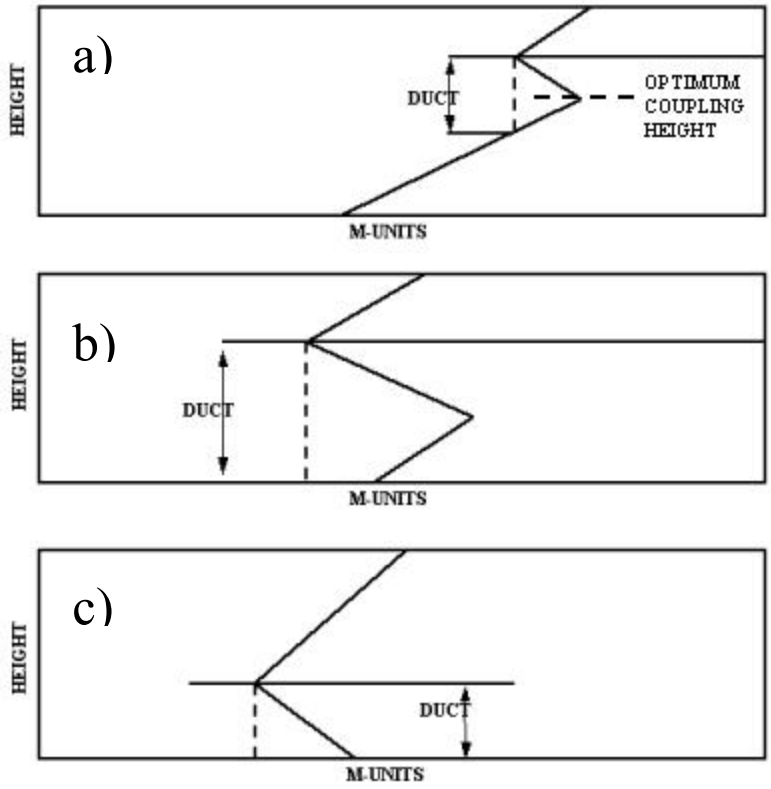


**Figure 3.2.** Effects of different M-profiles on ducting conditions. (a) Elevated duct (trapping layer elevated), (b) Surface-based elevated duct (trapping layer elevated), and (c) Surface duct (trapping layer on surface) [after Helvey et al., 1994].

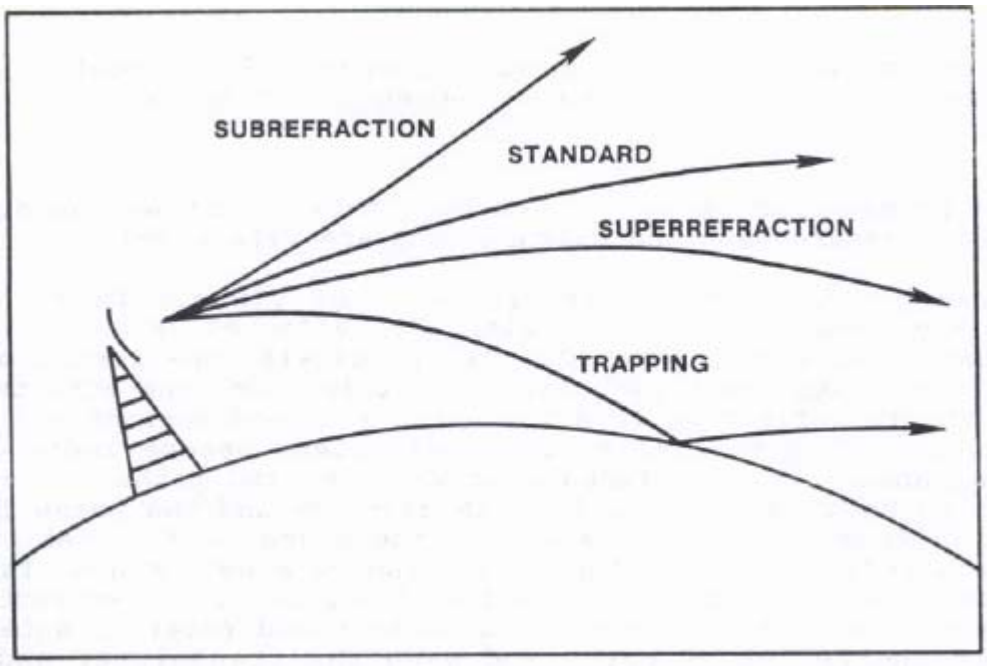


**Figure 3.3.** Possible radio wave propagation behaviors, including subrefraction, standard, super-refraction, and trapping (ducting) [Wave Propagation Panel, 1990].

### 3.2 Radio Physical Optics (RPO) Model

The Radio Physical Optics program does a good job of modeling the expected propagation loss for near-surface transmitters and paths that are entirely over water [Hitney, 1995]. The data that will be introduced in Chapter 4 comes from two places. One set is from the U.S.N.S. Sumner while it was located in the Gulf of Mexico and along the Atlantic coast of Florida, and the other is from data representing the Persian Gulf region. Because both sets are ocean-based, the RPO program should accurately represent the propagation that would occur based upon the refractivity measured by the LAPS lidar and by meteorological sondes.

RPO uses a combination of ray optics and parabolic equation techniques to efficiently arrive at propagation loss as a function of spatial dimensions, range and altitude. The ray optics model traces direct and reflected waves through a series of

"control points", and then determines the magnitudes of these waves, as well as the phase difference between them at each desired altitude and range. The properties of the input rays themselves are determined by user defined inputs, such as frequency, antenna height, elevation angle, and pattern [Hitney, 1992]. The parabolic equation method begins with Maxwell's equations and a defined complex field u(x,z). The field is then advanced to the next point u(x+δx,z) through the equation:

$$u(x+\delta x, z) = e^{jk\delta x[10^{-6}M(x,z)]}\Im^{-1}[U(x,p)e^{-jp2\delta x/2k}]$$

where,

k is the wavenumber,

M is the modified refractivity,

x is the range from the transmitter

z is the height from the transmitter

and,

$$p = k\sin(\theta),$$

$$U(x,p) = \Im[u(x,z)] = \int u(x,z)e^{-jpz}dz.$$

The field at u(x,z+δz) can be determined in a similar manner. The full details have been left out for simplicity, but are available [Dockery, 1988]. In order to achieve high efficiency, the range over which the ray optics model can be used accurately has been maximized in RPO. This is to avoid relying too much on the calculation-intensive parabolic equation method. The implementation of the program consists of specification of parameters in two separate files, one that determines the "system", and another that specifies the "environment".

The environment file allows a variety of options, such as surface temperature, specific humidity, attenuation of air, and wind speed [Hitney, 1995]. However, the necessary part of the input for the environment consists only of altitudes with corresponding M-values, which can be used to describe refractive conditions. The case studies presented in this thesis have focused on the M-values alone and emphasize ducting events. Additionally, the environment file provides the option to place a label at the top of each output graph.

The system file is more complex, and determines the specifications of the transmitter as listed below in Table 3.1 [Hitney, 1995]. Besides the items listed in the table, the system file also allows the used to specify the maximum height, maximum range, and color scale options for the graphic display.

The data from the Persian Gulf region came from a data set that was collected by Remcom, Inc [Steve Fast, private communication]. Therefore, the antenna characteristics that were chosen for this thesis are the same as those selected by Remcom, Inc. for an

**Table 3.1.** Parameter descriptions for RPO transmitter input.

| Parameter | Description |
|---|---|
| Frequency | Radar frequency from 100 to 20,000 MHz |
| Antenna Height | Height above sea level from 1 to 100 meters |
| Polarization | Horizontal, vertical, or circular |
| Antenna Pattern | Omni-directional, Gaussian, Sinc(x), Cosecant-Squared |
| Vertical Beamwidth | Beamwidth full angel between 3dB points |
| Elevation Angle | Beam angle above horizontal |

interesting case. The values chosen for most of the modeling process are listed in Table 3.2. These values were used when modeling radio-wave propagation in the coastal Florida/Gulf of Mexico region, as well as in the Persian Gulf. Additionally, a couple cases have been chosen to observe what the effects on propagation would be if the frequency were varied. Antenna frequencies of 3 GHz and 10 GHz were used for the USSA, 1976 model standard atmospheric conditions, as well as for conditions during a ducting event in the Persian Gulf. The graphs are shown at the end of the section, in Figures 3.7 through 3.10. Of note is the difference in antenna patterns between Figures 3.7 and 3.8. Because the frequency is higher in Figure 3.8, more constructive and destructive interference fringes occur, and a larger number of minima and maxima are seen in the same spatial region. The same difference in pattern is noticed when comparing Figures 3.9 and 3.10, but in these two graphs strong ducting occurs at the surface. As a result these two figures show increased propagation distance far beyond what is seen in Figures 3.7 and 3.8. An antenna height of 10 meters was chosen in all cases as a reasonable height for a radar to be placed on a Navy ship or at a coastal site.

In order to establish a basis for analysis, the average atmospheric conditions given in the United States Standard Atmosphere, [USSA, 1976] were extracted and processed to arrive at M-values for relevant altitudes in the troposphere. As an example of the outputs that RPO generates, the calculated refractivity and modified refractivity profiles shown in Figures 3.4 and 3.5 for the conditions of the USSA76 model atmosphere have been used to calculate the RPO output for the radar specified in Table 3.2, and the result is shown in Figure 3.6. The model atmosphere results in the smooth refraction profiles and uniform propagation conditions as expected. Distance from the transmitter is

displayed on the x-axis, and altitude is on the y-axis. White space indicates negligible radio wave propagation, and thus we observe that the radio waves generated by USSA76 conditions produce no long-range surface propagation. Also, the effect of Earth's curvature is clearly seen in Figure 3.6.

**Table 3.2.** Values used for transmitter design in RPO model.

| Parameter | Description |
|---|---|
| Frequency | 1000 MHz |
| Antenna Height | 10 meters |
| Polarization | Vertical |
| Antenna Pattern | Omni-directional |
| Vertical Beamwidth | 2 degrees |
| Elevation Angle | 0.5 degrees |

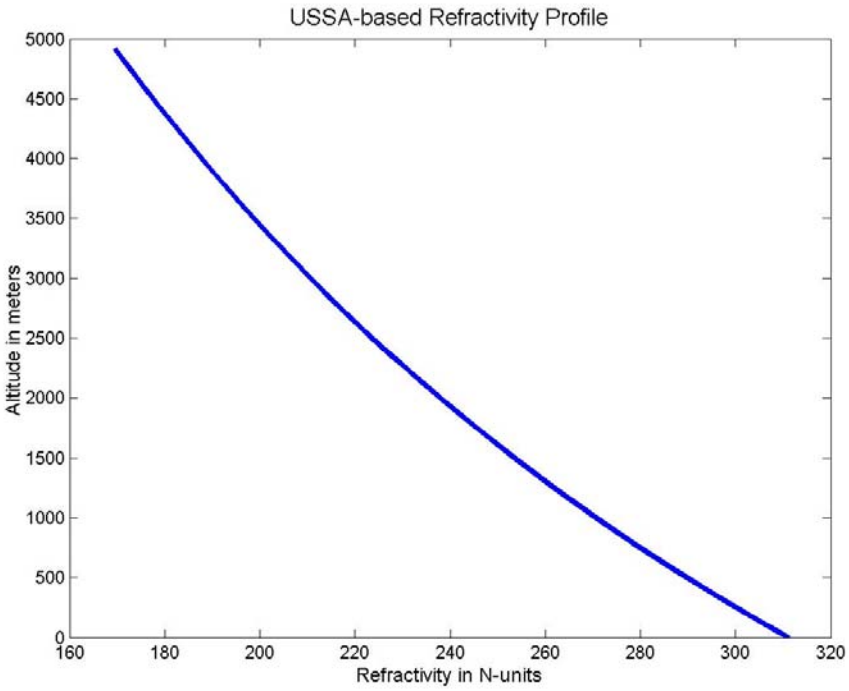


**Figure 3.4.** United States Standard Atmosphere refractivity profile in N-units.

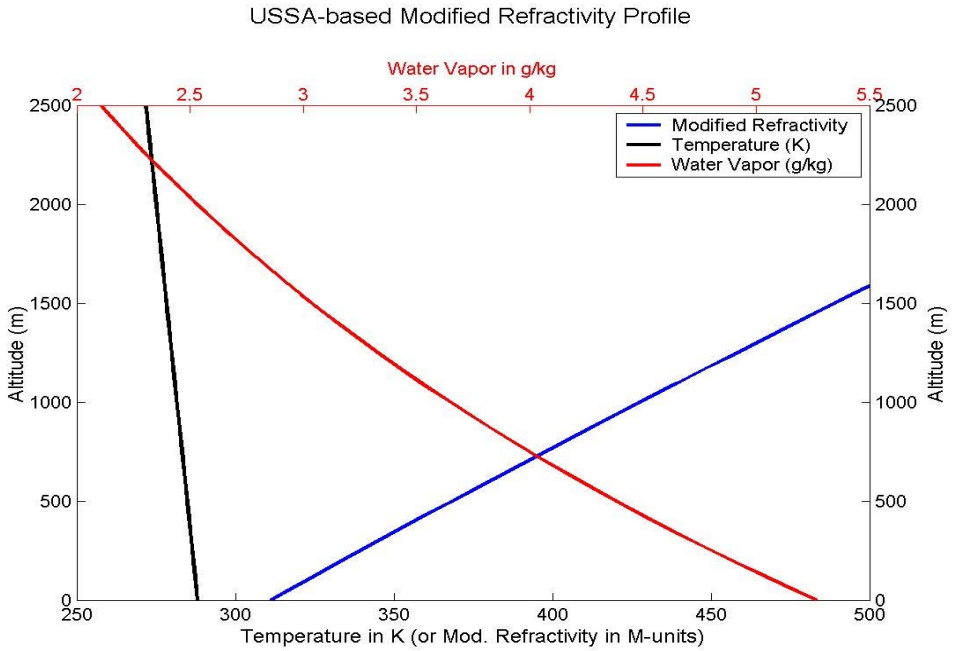


**Figure 3.5.** United States Standard Atmosphere modified-refractivity profile in M-units. Standard specific humidity and temperature are included.

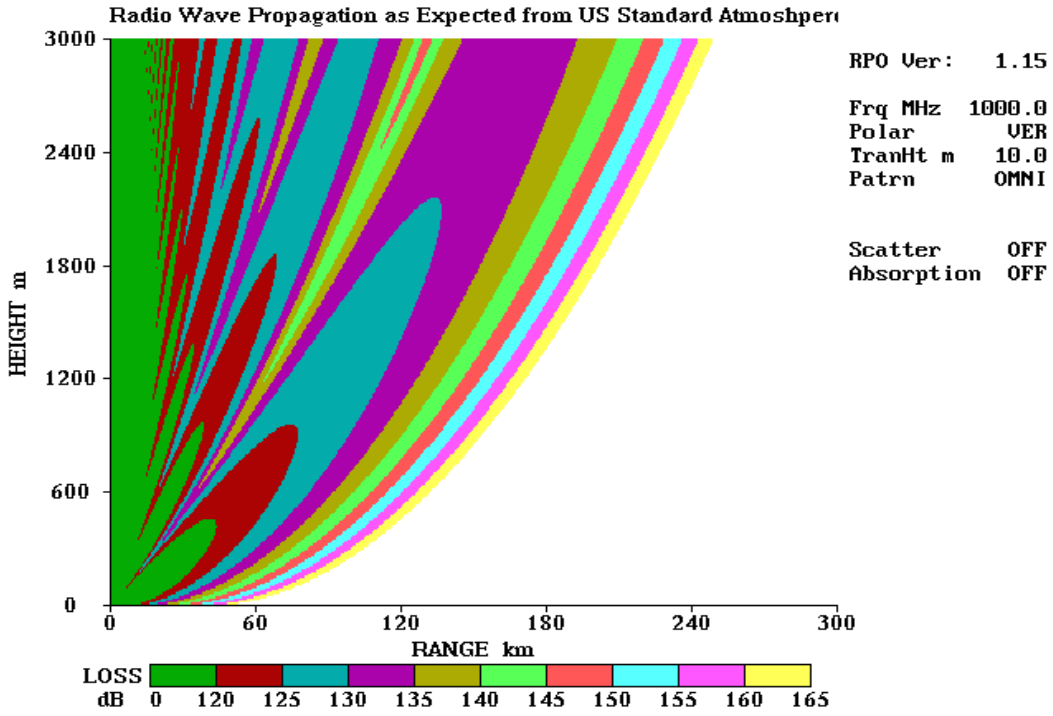


**Figure 3.6.** RPO output generated from USSA conditions, showing no ducting.

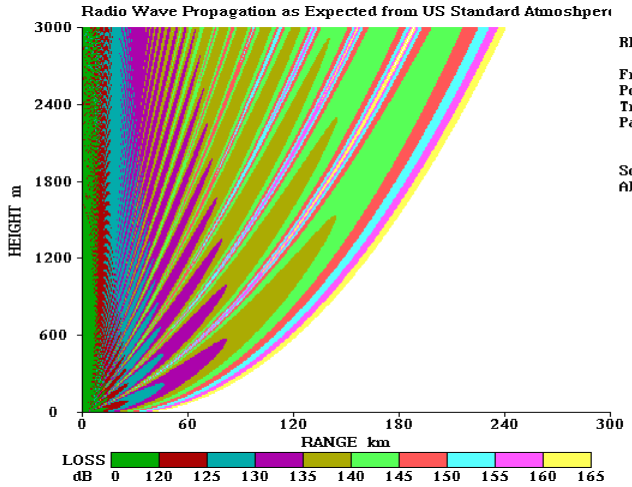


**Figure 3.7.** RPO model for 3 GHz antenna, USSA conditions.

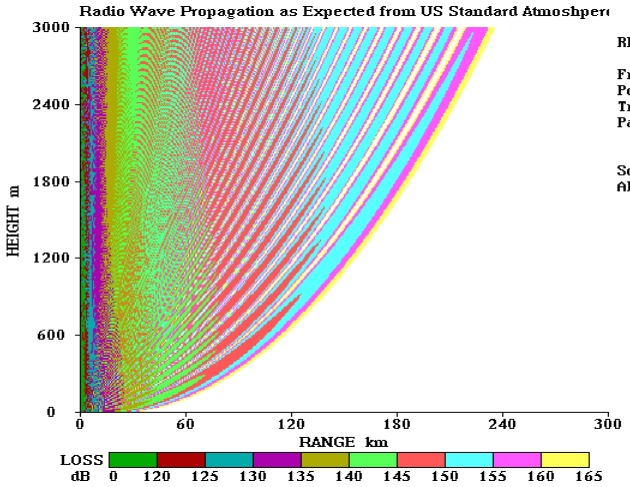


**Figure 3.8.** RPO model for 10 GHz antenna, USSA conditions.

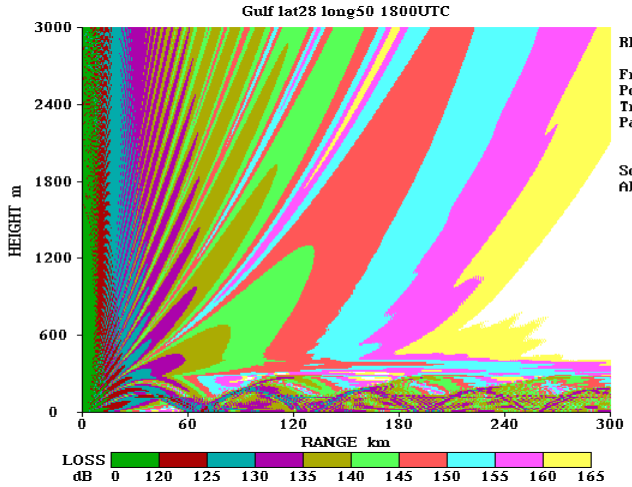


**Figure 3.9.** RPO model for 3 GHz antenna in Persian Gulf.

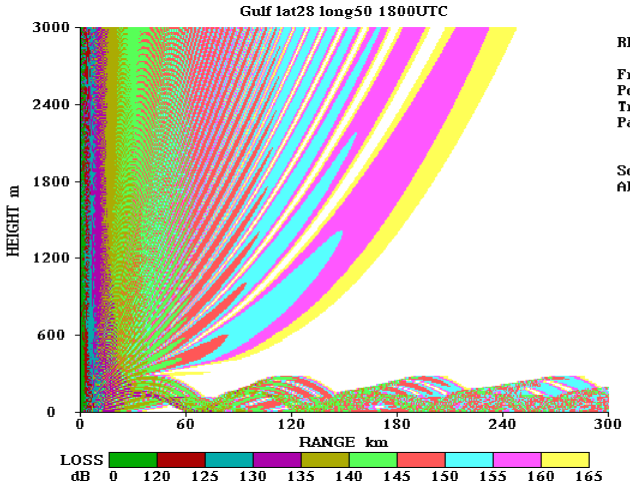


**Figure 3.10.** RPO model for 10 GHz antenna in Persian Gulf.

### 3.3 Integrated Refractive Effects Prediction System (IREPS) Model

In the years prior to the release of RPO, a refractivity modeling program called Integrated Refractive Effects Prediction System (IREPS) was released by the Naval Ocean Systems Center. The program was developed at NOSC "to provide a shipboard environmental data processing and display capability for the comprehensive assessment of refractive effects upon naval surveillance, communications, electronic warfare, and weapon-guidance systems" [Patterson, 1990]. Although this thesis will not focus on the outputs from IREPS, as it is somewhat antiquated and its calculations are less accurate, this model does have a few interesting features that should be pointed out.

IREPS can use the same inputs as the RPO model for defining the antenna and the "environment" data for the model, and will use the same M-unit values at corresponding altitudes. In addition, IREPS allows the environment data to be input by giving N-unit values or by directly providing the radiosonde (temperature, water vapor, and pressure) values. The most striking difference that one immediately notices is how the electromagnetic propagation plots are displayed. IREPS shows less detail than RPO regarding propagation loss, but it does show the natural curvature of the Earth, which provides a better initial picture of how a ducted wave propagates. Figure 3.11 shows an IREPS output for the U.S. Standard atmosphere, while Figure 3.12 shows a propagation output for a particularly interesting ducting case in the Persian Gulf region in August 2003. The same inputs were used for Figures 3.5 and 3.6, so a comparison of the two models for the USSA can be made; the main feature of notice is how the two programs handle the Earth's curvature. In RPO, the radio wave seems to curve upward from a flat

surface, but viewing the IREPS output shows the actual case, that of a curving earth and a wave that travels straight, resulting in a natural increase in altitude with distance.

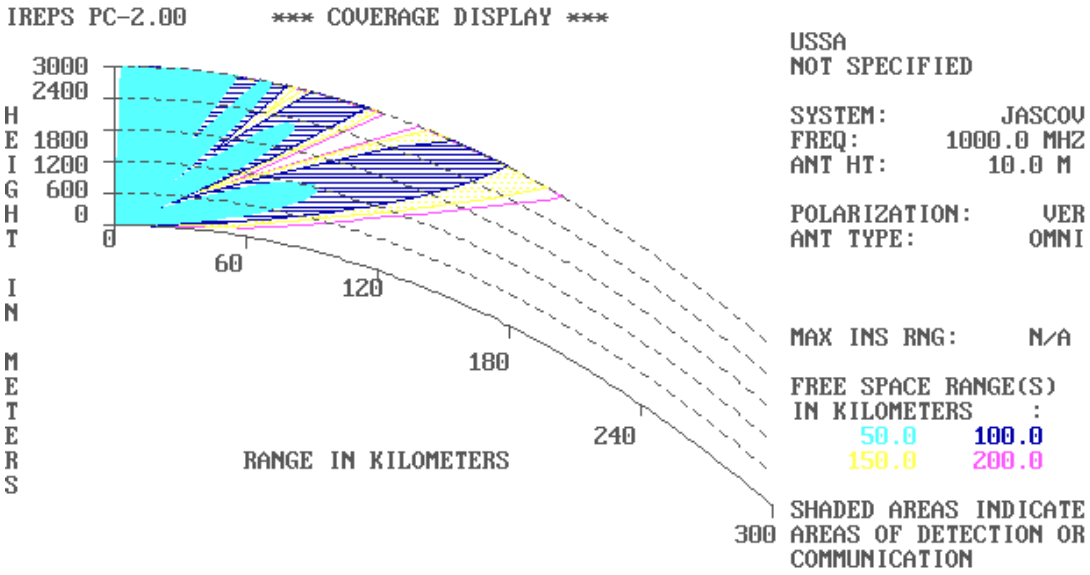


**Figure 3.11.** IREPS output for USSA conditions, given radar specifications in Table 3.2 and corresponding to the RPO output presented in Figure 3.6.

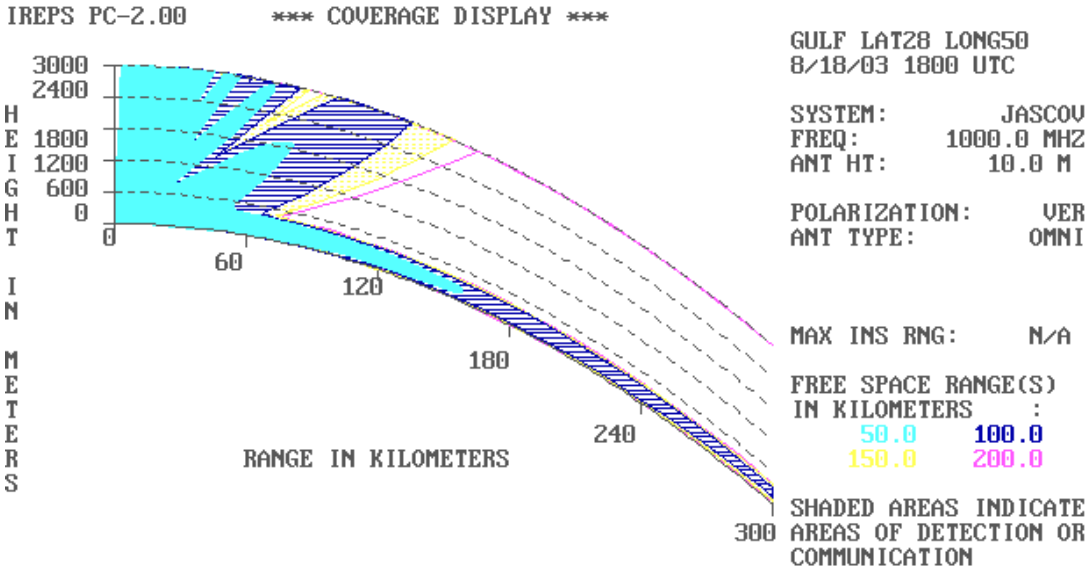


**Figure 3.12.** IREPS output for ducting case in Persian Gulf, 28 degrees latitude and 50 degrees longitude, on 8/18/03 at 1800 UTC and corresponding to the RPO output presented in Figure 3.9.

# CHAPTER 4

## CASE STUDIES OF ATMOSPHERIC EFFECTS ON RADIO-WAVE PROPAGATION

The objective of this chapter is to illustrate the advantages of having ocean-based sensors, namely lidar instruments, which could provide continuous real-time meteorological measurements, and therefore refractivity profiles. It will be shown that having just a few lidar systems available on Navy ships in a region would be enough to provide an accurate description of radio-wave propagation in that region, or littoral area. Data will be examined from two geographical regions to demonstrate this point. Data were taken by the Penn State LAPS lidar aboard the U.S.N.S. Sumner, in the Gulf of Mexico/coastal Florida region (shown in Figure 4.2), and these data provide the perspectives gained from using such a system. The data in the Persian Gulf region were obtained from a MM5 (Mesoscale Model, Version 5) forecast provided by the AFWA (Air Force Weather Agency), and the data used in the model were obtained from radiosonde measurements in Iraq, Iran, Saudi Arabia, and Kuwait [Steve Fast, private communication]. The results from the model provide the meteorological environment for the Persian Gulf, off the coasts of Qatar, Bahrain, Saudi Arabia, and Kuwait. The conditions observed in this region exemplify very severe ducting. The Gulf region is shown in Figure 4.1.

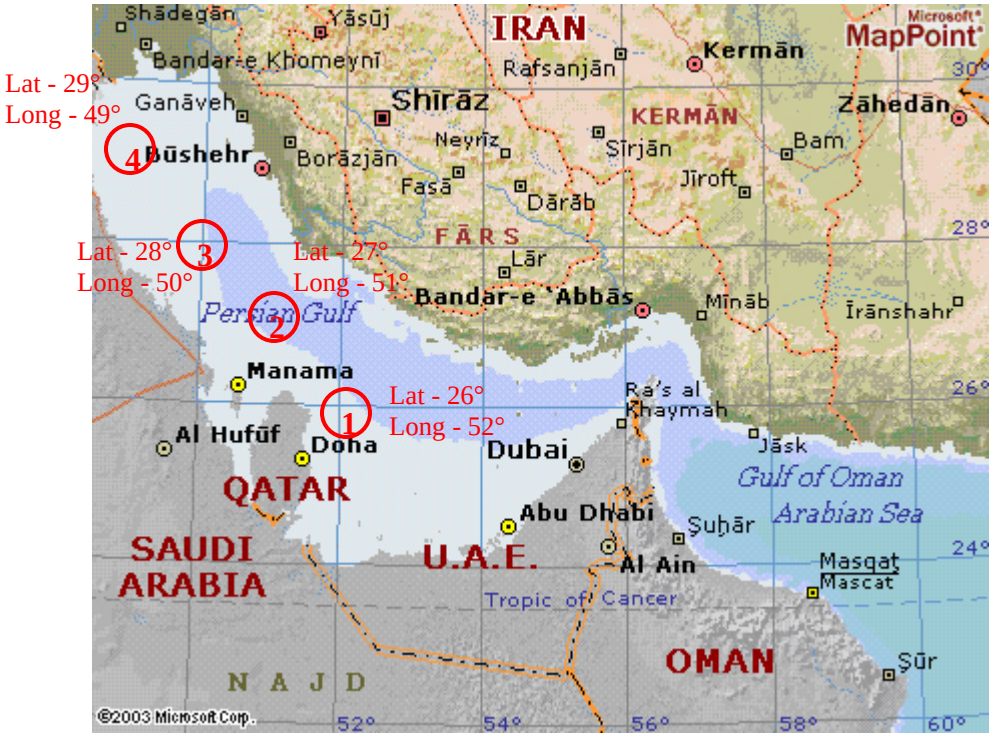


**Figure 4.1.** Map of the Persian Gulf. Weather data comes from locations indicated by the circles [http://www.persiangulfonline.org/maps.htm].

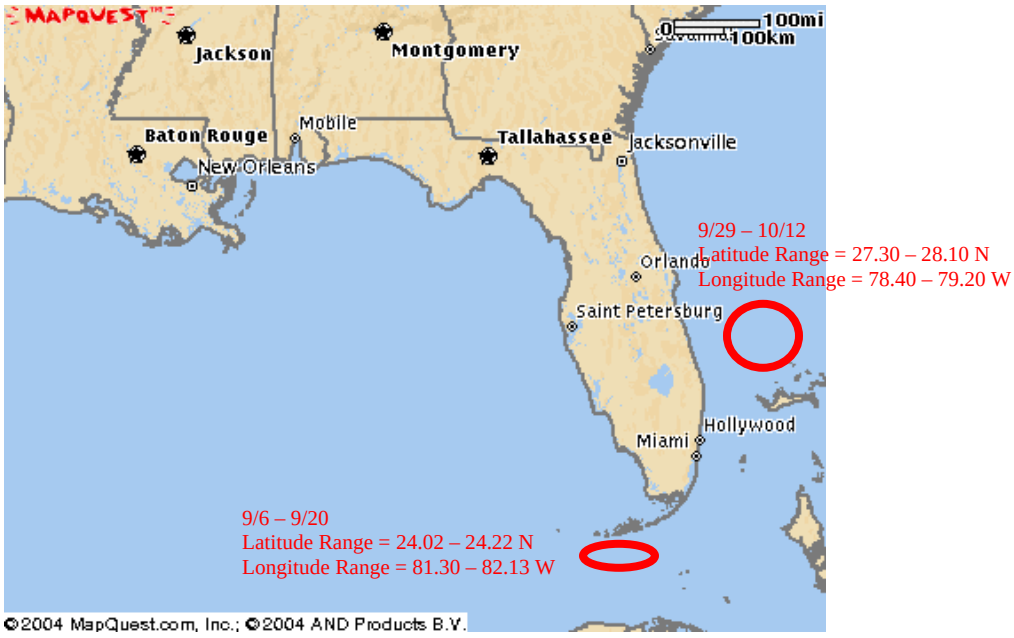


**Figure 4.2.** Map of the Gulf of Mexico/Florida coastal region. The data used in the analysis shown in subsequent figures were taken within the regions indicated by circles [www.mapquest.com].

### 4.1 Development of the RF Refractivity Ratio

A typical time sequence of modified RF refractivity, which was calculated from measurements taken by the LAPS lidar, is shown in Figure 4.3. Using this type of plot makes it somewhat difficult to quickly locate ducting conditions, and this is the motivation behind developing an alternative way to examine refractivity profiles taken by lidar systems. The method involves taking the ratio of the lidar measurements to the refractive values expected for the conditions of the United States Standard Atmosphere, which represents the global mid-latitude mean.

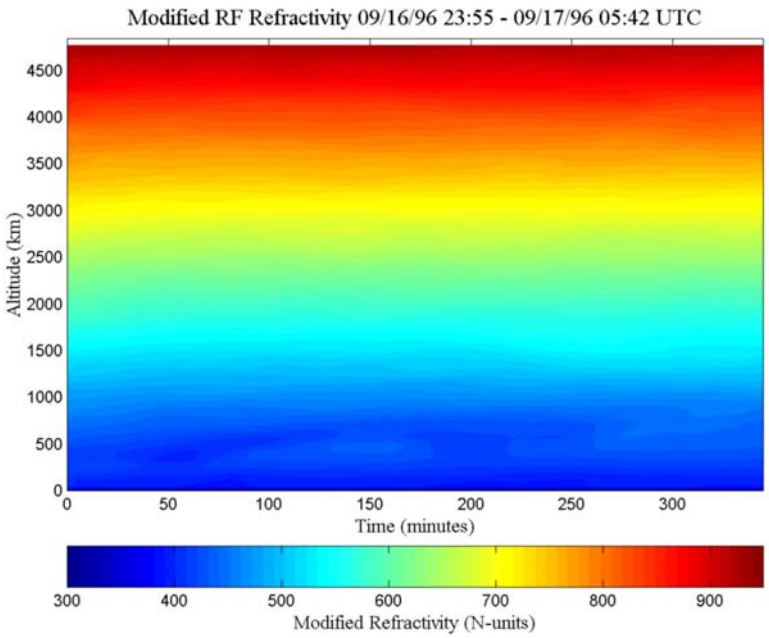


**Figure 4.3.** Typical modified refractivity time sequence calculated for the measurements made by the LAPS instrument.

#### 4.1.1 United States Standard Atmosphere, 1976

The USSA, 1976, was prepared to provide a useful reference model of the variables that make up the mean values for the mid-latitude atmosphere. Its main

offering is a complete list of average values for many variables throughout the height range of our atmosphere. These values are given from -5 to 1000 km in altitude, relative to sea level. Variables included are temperature, pressure, density, acceleration due to gravity, pressure scale height, number density, particle speed, collision frequency, mean free path, molecular weight, speed of sound, dynamic viscosity, kinematic viscosity, and thermal conductivity. Additionally, mean concentrations are given for certain trace constituents in the lower atmosphere. There are many included, but those of interest to us are ozone and water vapor content, two of the species that are measured by the Penn State LAPS lidar instrument. The USSA also gives equations and summaries from measurements of the meteorology, including subjects like scale height, mean air-particle speed, mean free path, mean collision frequency, and number density. Finally, the publication includes comparisons between the models used and sets of measurements [United States Standard Atmosphere, 1976].

Calculating the RF refractivity based on the information in the USSA requires relative humidity, temperature, and pressure, all of which can be found in the publication. However, since the altitudes given in the USSA do not match those at which data are taken with the LAPS instrument, an interpolation analysis was performed. This was done using Microsoft Excel, and the graphs are shown in Figure 4.4. The pressure and water vapor values were fit to a log scale, while the temperature values were fit to a linear scale. The $R^2$ values are all above 0.99, and reinforces the idea that the equations given on the graphs are adequate for calculating the variables at any height below 5000 meters. Note that use and interpolation of the USSA water vapor data results in a smoothed moisture graph through the boundary layer. This is the area that one would normally

expect to see water vapor gradients, but these gradients are not seen because the values shown are global averages. The end result is that with the interpolated values, an accurate ratio of LAPS versus USSA values can be taken. Figures 3.3, 3.4, and 3.5 show the calculated N and M profiles, as well as the RPO propagation results from the USSA76 model.

### 4.1.2 The RF Refractivity Ratio

As earlier stated, an interesting way of examining refractive conditions is through using the ratio of refractivity measurements to the values derived from the USSA76. Time sequences of profiles of modified refractivity show such little variation with altitude, that it is difficult to pick out features of interest. Figures 4.5a and 4.5b show time sequences of data taken on September 11, 1996, while Figures 4.5c and 4.5d display time sequences of data taken on September 1, 1996. The two graphs on the left plot the ratio, while the graphs on the right plot only the measured modified refractivity. It should be noted that typical surface values of water vapor aboard the U.S. Sumner during the 1996 campaign were between 15 and 20 g/kg, which is 3-4 times the average value of the US Standard Atmosphere. This is the reason that the ratio near the surface is higher.

From visual inspection, it is immediately obvious that the ratio profiles permit better discrimination of the regions of refractive gradients. In Figure 4.5a, a layer of increased refractivity ratio appears around 1500 meters. Figure 4.5b, showing only the modified refractivity, does not display such a phenomenon at 1500-meters altitude. Comparisons of Figures 4.5a and 4.5b with Figures 4.5c and 4.5d provide another dimension to the argument. The modified refractivity profile for September 1, 1996,

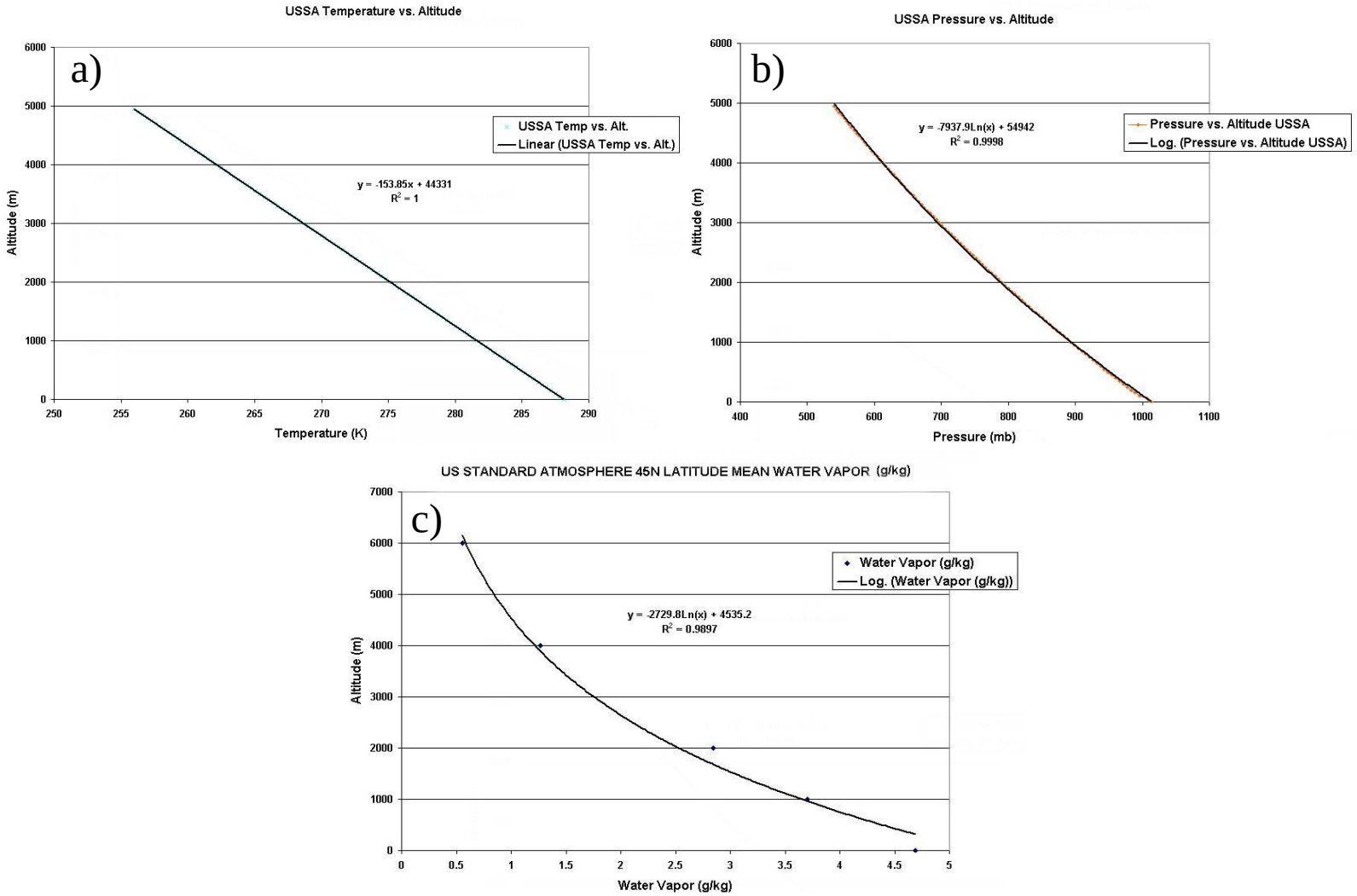


**Figure 4.4.** Graphs of the parameters from the USSA regression line fitting. (a) Temperature, (b) Pressure, (c) Water Vapor.

appears nearly identical to the one on September 11, yet the ratio plots for each day exhibit significant differences. While much more evidence exists to support this claim, a quick examination of these four graphs will verify that the ratio plots provide more useful information on the refractive gradients for visual inspection. The end result is that a quick and easy visual determination can be made to find where ducting conditions may exist, so that a more thorough examination may ensue. A few examples of the value of these ratio plots will be shown in Section 4.2.

### 4.2 Lidar Measurements of Ducting Conditions

Although the lidar data taken aboard the U.S.N.S. Sumner in 1996 does not provide any examples for major ducting conditions, a few interesting cases do arise, and the plots demonstrate that the lidar data provides a good analysis tool. One case of a surface duct and a couple cases of elevated ducts are shown as examples from the U.S.N.S. Sumner. Section 4.3 will present the results from the Persian Gulf region that show examples of ducting conditions in a region of strong refraction.

The first example of ducting selected from the LAPS lidar data is an elevated duct on September 17, 1996. Figure 4.6 shows the modified refractivity ratio profile for this date, which was calculated using the method described in Section 4.1. It should be noted that the lidar profiles shown in this thesis are based on 1-minute data with 5-minute integration. This particular profile shows a sharp decrease in the ratio in the 500-700 meter altitude range. Examining this further, Figure 4.7 shows a profile of temperature, water vapor, and modified refractivity during the middle of the time period shown in the ratio plot. It is seen that a decrease in water vapor, from about 18 g/kg to 11 g/kg, occurs

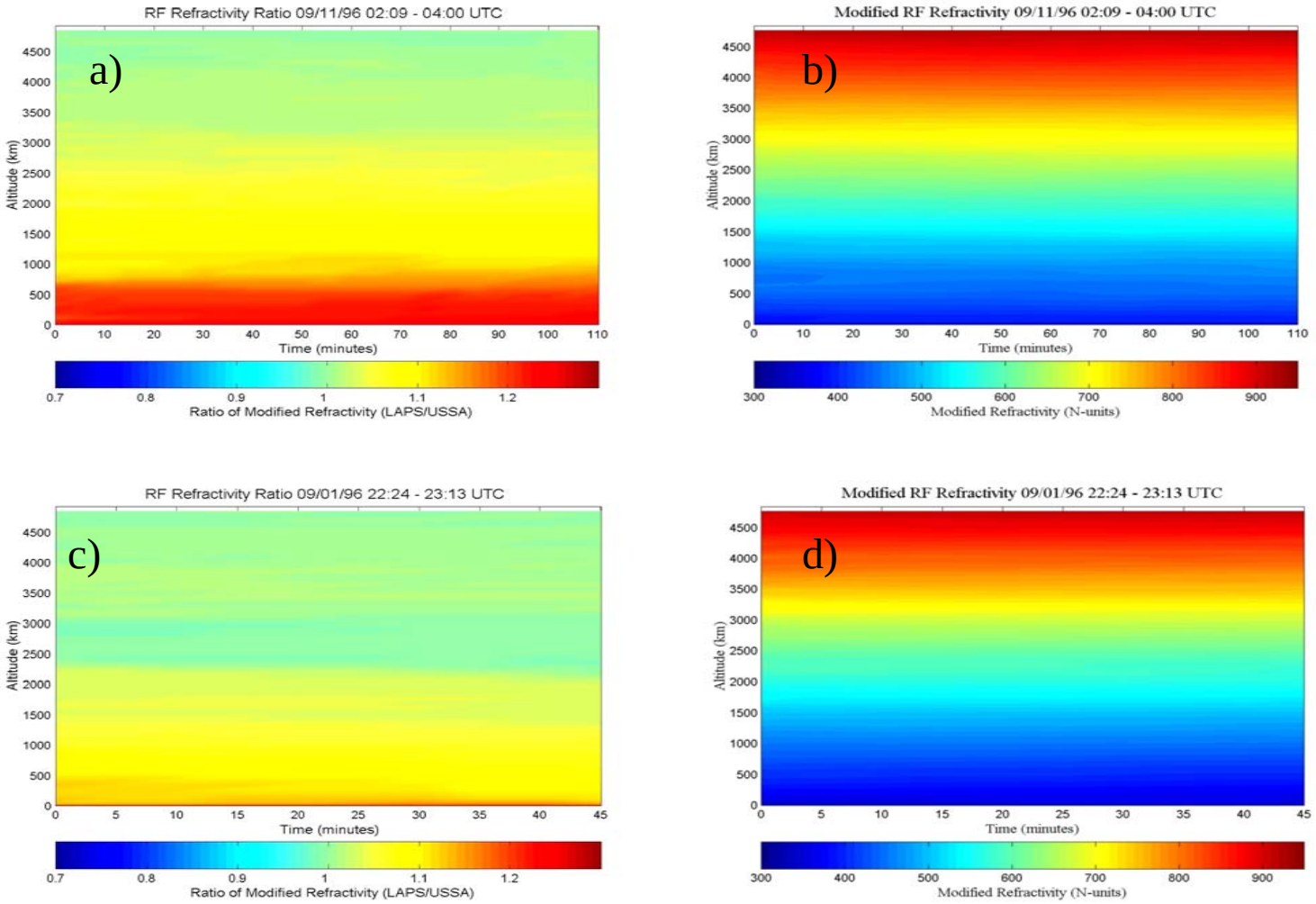


**Figure 4.5.** Comparisons of LAPS data taken on September 11, 1996 (a) refractivity ratio and (b) modified refractivity with September 1, 1996 (c) refractivity ratio and (d) modified refractivity.

between 500 meters and 700 meters in altitude. The overall effect is that of an elevated duct at 550 meters, with a thickness of about 200 meters. The M-unit differential in the duct is small, at about 15 M-units, indicating a relatively weak duct. The optimum coupling height can be seen to occur at 500 meters. In order to understand how a small duct like this might affect radio-wave propagation, the RPO model was run with the same data used to generate Figure 4.7, and the result is shown in Figure 4.8. In an attempt to capture what may happen in this situation for an aircraft radar, the antenna height was placed at the maximum altitude possible in RPO, 100 meters, which is 400 meters below from the desired height. Despite the fact that the desired situation could not be recreated, at 500 meters a bend in the attenuation is displayed. Comparing this to Figure 4.9, in which the antenna height is 10 meters, does not show that the more elevated antenna has a large increase in radio wave refraction, but it does show an effect in the interference pattern.

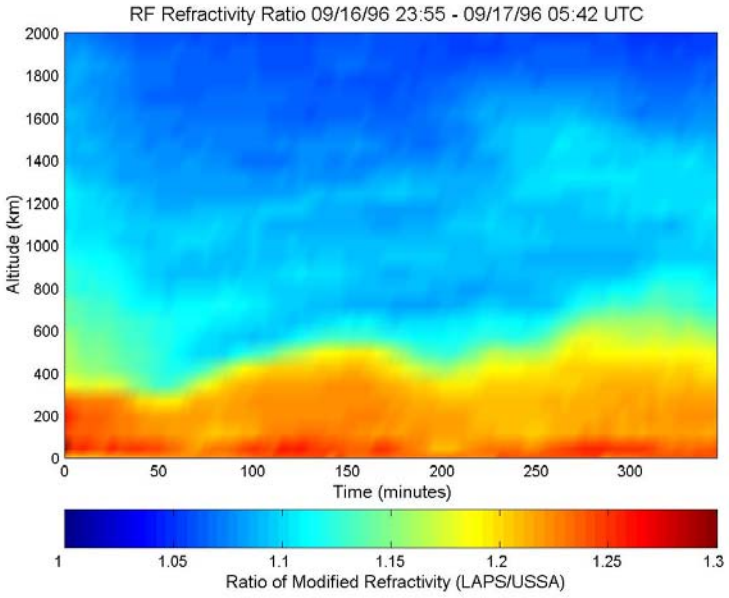


**Figure 4.6.** LAPS modified refractivity ratio showing large gradient around 500 meters.

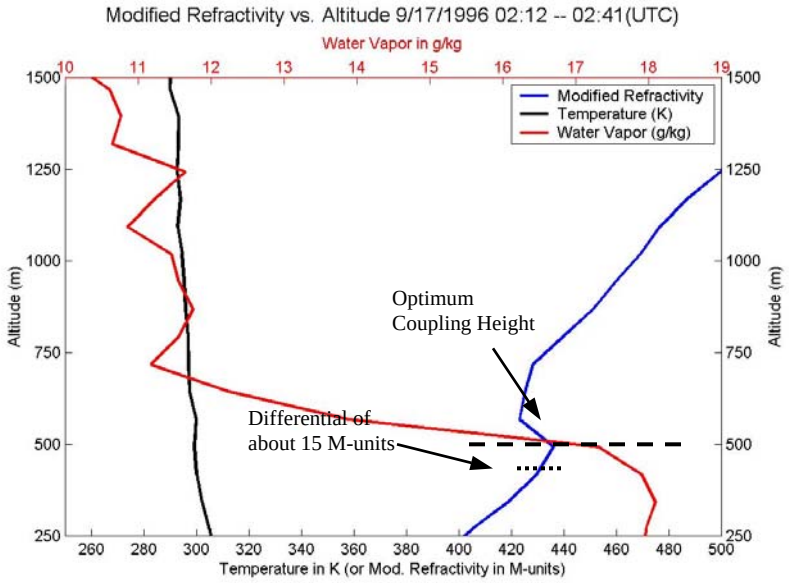


**Figure 4.7.** LAPS profile showing temperature, water vapor, modified refractivity, optimum coupling height of the duct, and M-unit differential.

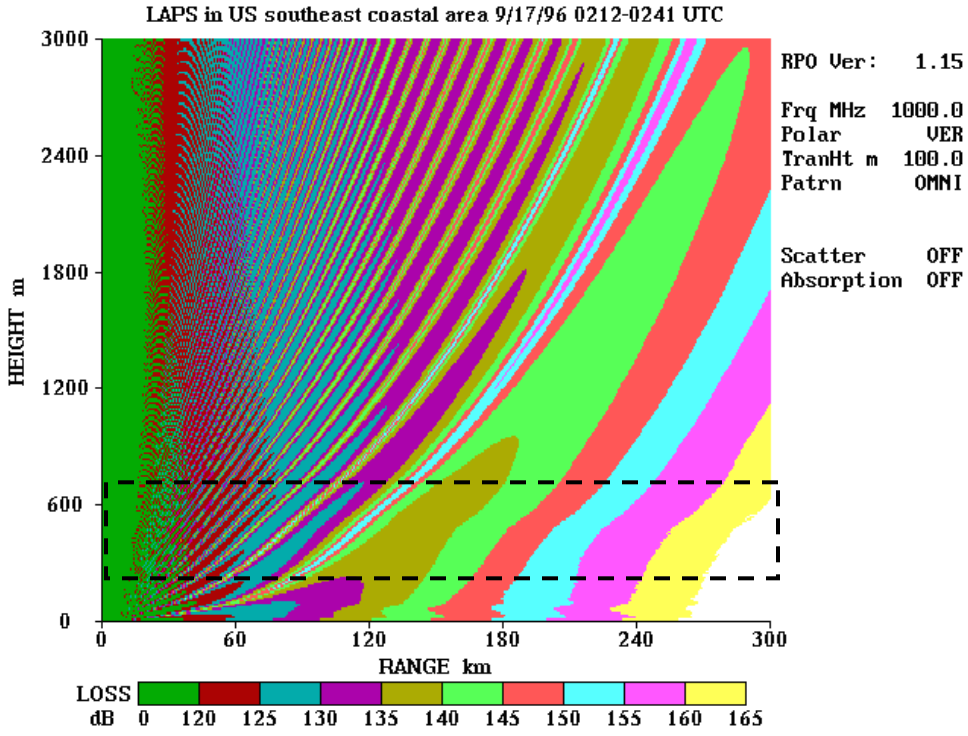


**Figure 4.8.** RPO output showing the effects of a small duct measured by LAPS on Sept. 17, 1996, near 500 meters altitude with antenna height placed at 100 meters.

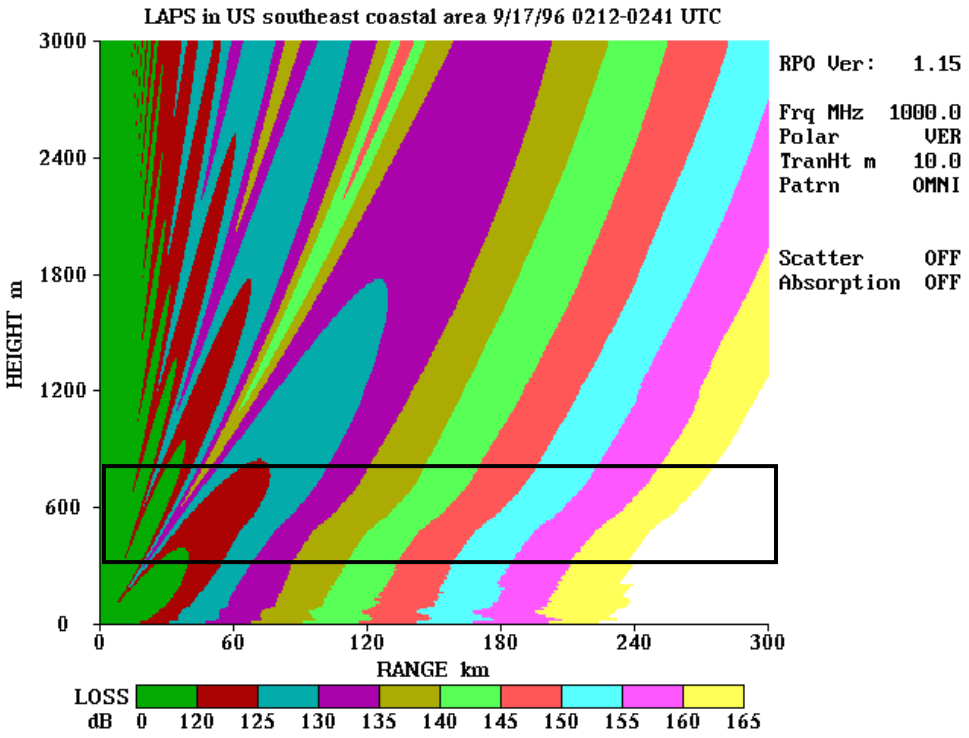


**Figure 4.9** RPO output showing the effects of a small duct measured by LAPS on Sept. 17, 1996, near 500 meters altitude with antenna height placed at 10 meters.

It is expected that placing the antenna at 500 meters altitude would cause trapping to occur. The results do suggest, however, that although the refractive conditions implied in Figure 4.7 are not enough to trap the radio waves when the antenna is not located in the duct, they are enough to cause the waves to be deflected outward, and an increased distance of propagation above that critical height results compared with the standard atmosphere (see Figure 3.5). This elevated duct would not be of much concern for a ship radar but would cause problems for aircraft radar.

The second example is another elevated duct, occurring between 1.5 and 2 km. Viewing the ratio profile in Figure 4.10 immediately brings this area to attention. A profile shown in Figure 4.11 shows a decrease in water vapor concentration, accompanied by an increase in temperature from about 1.7 to 2 km. Once again, these

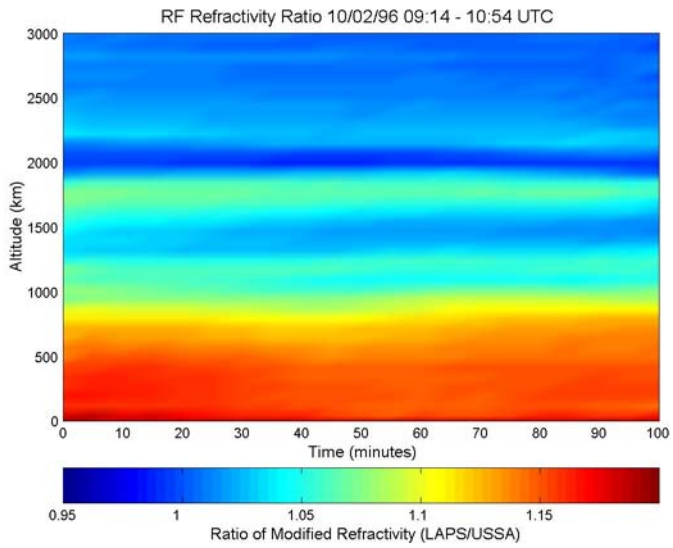


**Figure 4.10.** Refractivity ratio from LAPS Oct. 2, 1996, showing layer around 1.7 km.

trends produce a prominent elevated duct. The implications of the elevated ducts can be realized for either long-range detection of aircraft or missiles when using aircraft radar, or used passively as a listening post for aircraft ascending or descending through the duct at great range.

The final example from the U.S.N.S. Sumner is perhaps the most interesting. The profile in Figure 4.12 shows a small surface duct and the conditions that caused it. A significant temperature inversion is seen near the surface. Because of the LAPS instrument's telescope form factor, near-surface error in temperature measurements can occur, so a magnified graph of the temperature, accompanied by error bars is shown in Figure 4.13. Although a significant error bar is shown at 57 meters (the first range bin for the LAPS instrument), this point fits into a linear fit with the ground-based temperature sensor measurement and the second LAPS point. For this reason, the temperature inversion seen can be accepted as accurate. Figure 4.12 also shows a 2 g/kg decrease in water vapor over the first 57 meters. The combination of water vapor

decrease and temperature increase sets the conditions to expect a moderate duct near the surface in this unique case. Note that cases such as the one in Figure 4.12, result in the "optimum coupling height" at the surface and can be seen by observing the relative maximum M-value in the modified refractivity profile.

Using the modified refractivity values derived from the LAPS measurements, see Figure 4.12, a model was run in RPO to determine the effect that this small surface duct would have on radio propagation, and the result is shown in Figure 4.14. Although extreme refraction of the waves does not occur, the duct is strong enough to cause significant radio signal propagation to 300 km. Between surface to about 50 meters, red and blue streaks are seen, indicating a loss of only 120 to 130 dB, and this corresponds to a fairly strong signal traveling great distances.

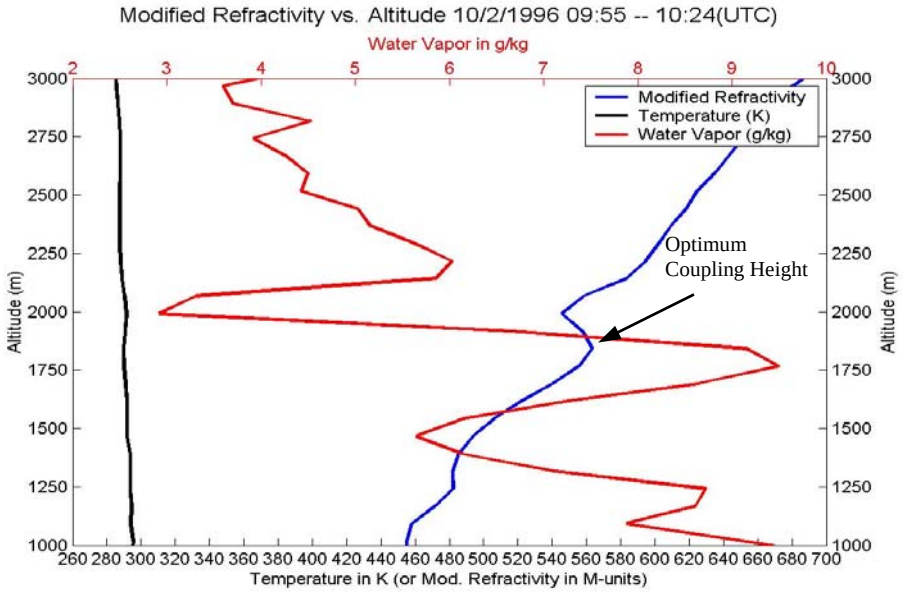


**Figure 4.11.** LAPS profile from Oct. 2, 1996, showing elevated duct and its causes.

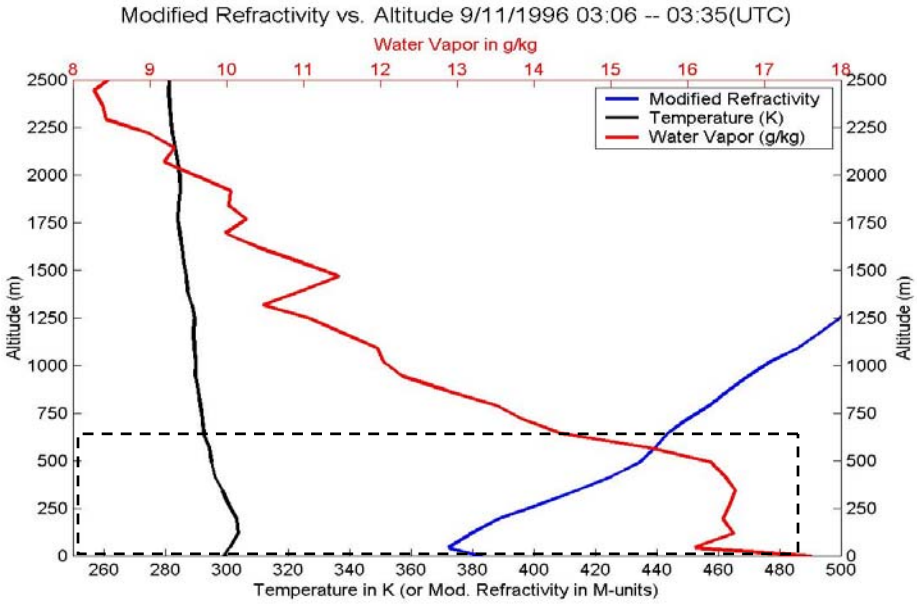


**Figure 4.12.** LAPS profile from Sept. 11, 1996, showing surface duct. Optimum coupling height occurs at surface.

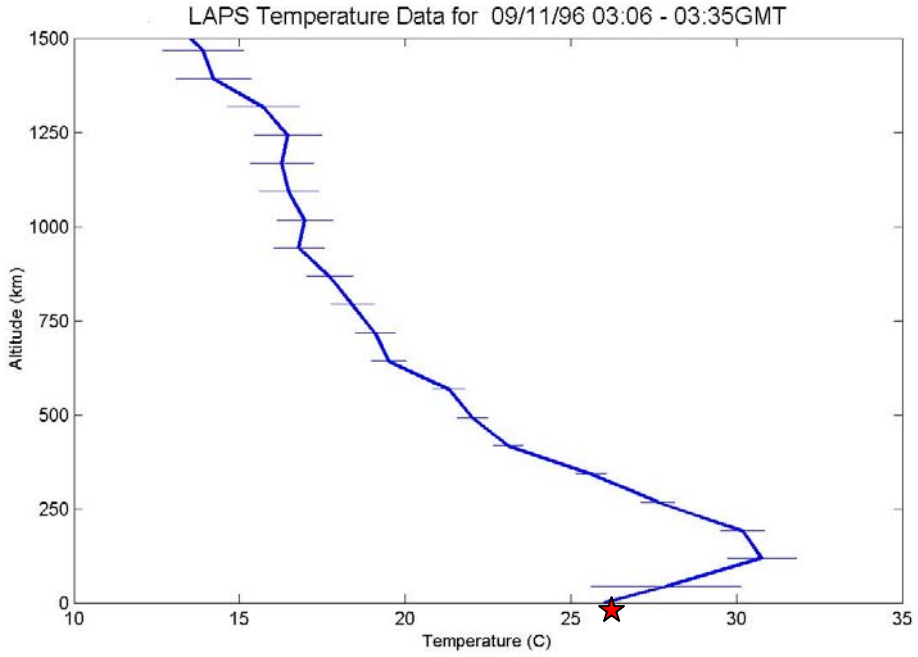


**Figure 4.13** Graph showing temperature inversion measured by LAPS instrument, with error bars, and star denotes that a temperature sensor measured the ground point.

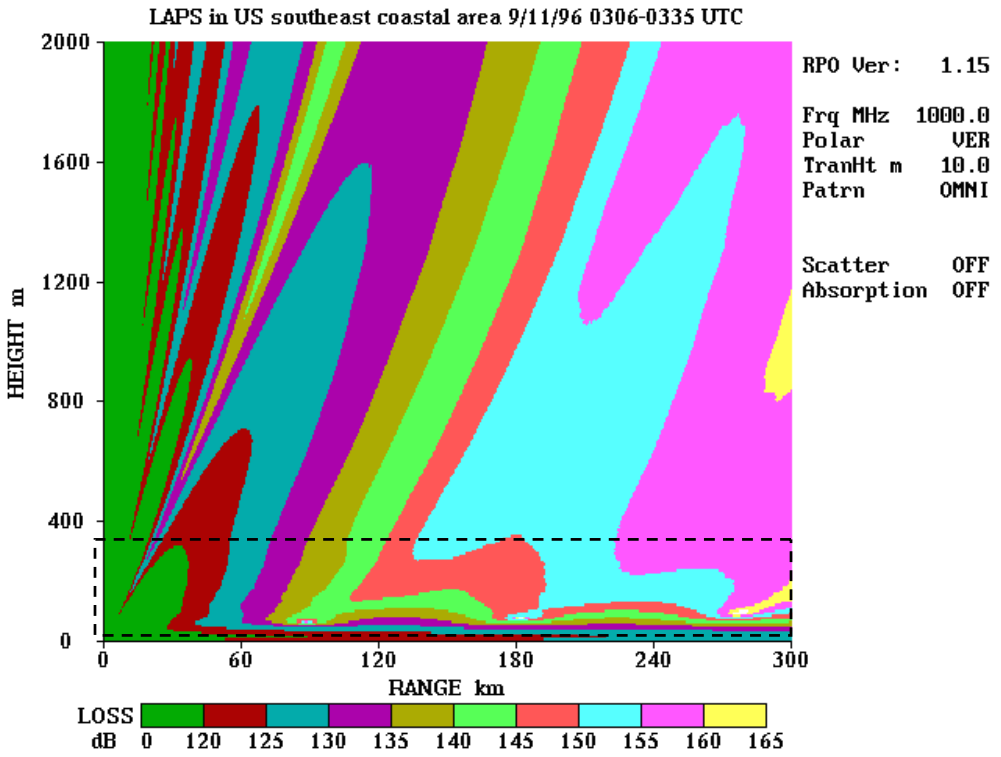


**Figure 4.14.** RPO output showing the effects of a surface duct on radio propagation during conditions measured by the LAPS lidar on September, 11, 1996.

### 4.3 Refractivity in the Persian Gulf and its Implications

Conditions that cause ducting of radio waves occur more readily in the Persian Gulf than in the Gulf of Mexico and East Coast region of the United States, and the severity of the ducting is much greater during mid-summer compared to autumn conditions. For this reason, there was an interest in studying the Persian Gulf region. Remcom Inc., a company located in State College, Pennsylvania, obtained weather data for the Persian Gulf for August 18, 2003 in 4 different locations. The locations are shown and labeled in Figure 4.1. At each location, profiles were provided at 03:00, 09:00, 12:00, 15:00, 18:00, and 21:00 UTC. The profiles were processed through

MATLAB programs and analyzed to determine where and when ducting conditions existed. Additionally, Excel spreadsheets were used to examine temporal and spatial variations in the refractivity profiles. Propagation conditions in the region were modeled using RPO and the results are shown in the following figures.

In Figure 4.15, all four locations at 03:00 UTC show the characteristic decrease in water vapor concentration accompanied by an increase in temperature with altitude just above the surface. However, as the location of the observations moves farther north and west, the magnitude of the water vapor gradient decreases. In fact, at the most northwest location, 29° latitude and 49° longitude, the specific humidity and temperature gradients become small enough that the surface-based elevated duct observed at the other three locations does not exist. Figure 4.16 shows that ducting of radio waves calculated from the RPO model occurs in the first three locations, while in the fourth, the strong ducting conditions have disappeared. Observations seem to suggest that the ducting phenomenon in the region is centered near 27° latitude and 51° longitude, and decreases outward from there.

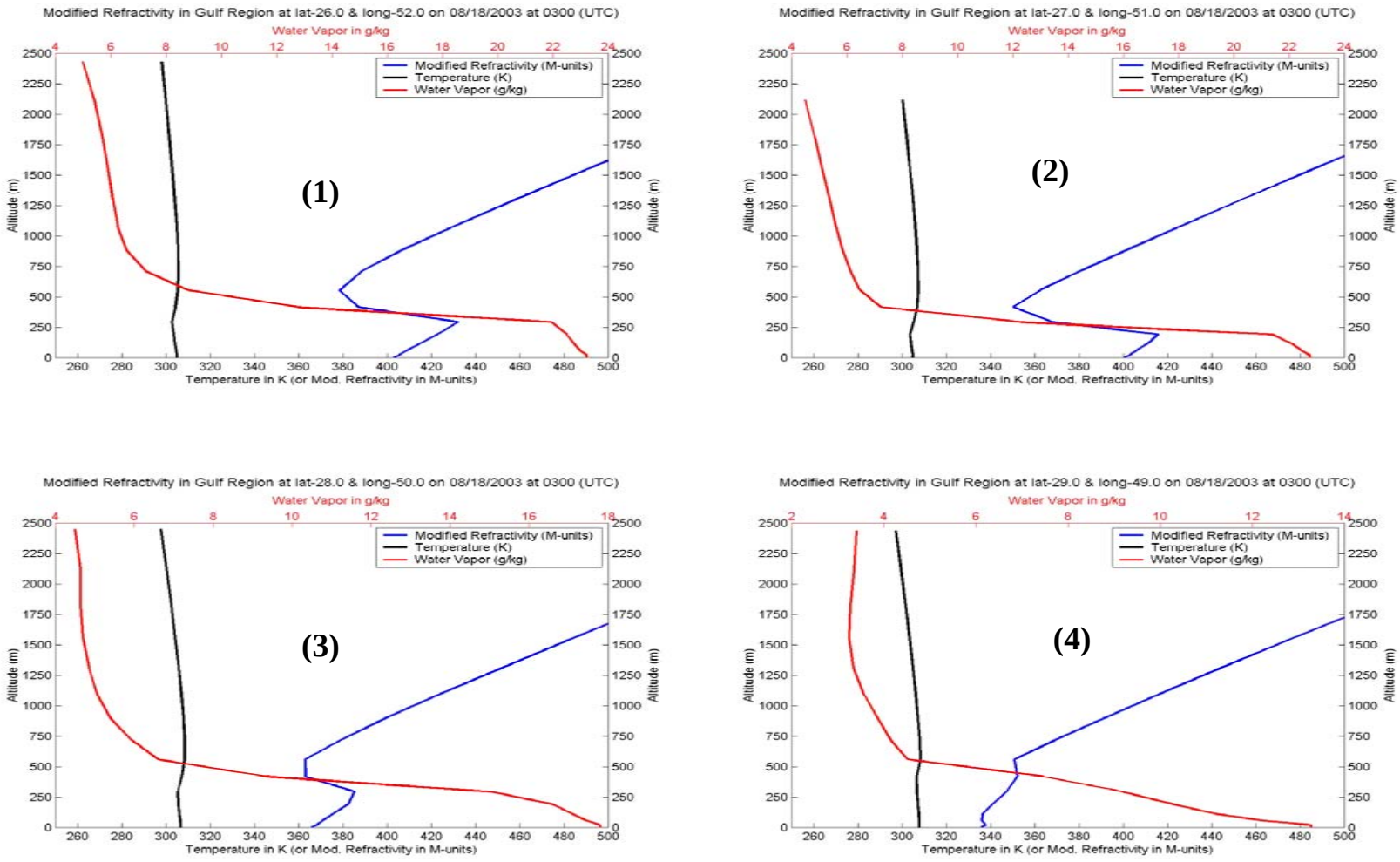


**Figure 4.15.** Gulf region profiles at 03:00 UTC show ducting in 3 out of 4 locations where the numbers refer to locations in Figure 4.1.

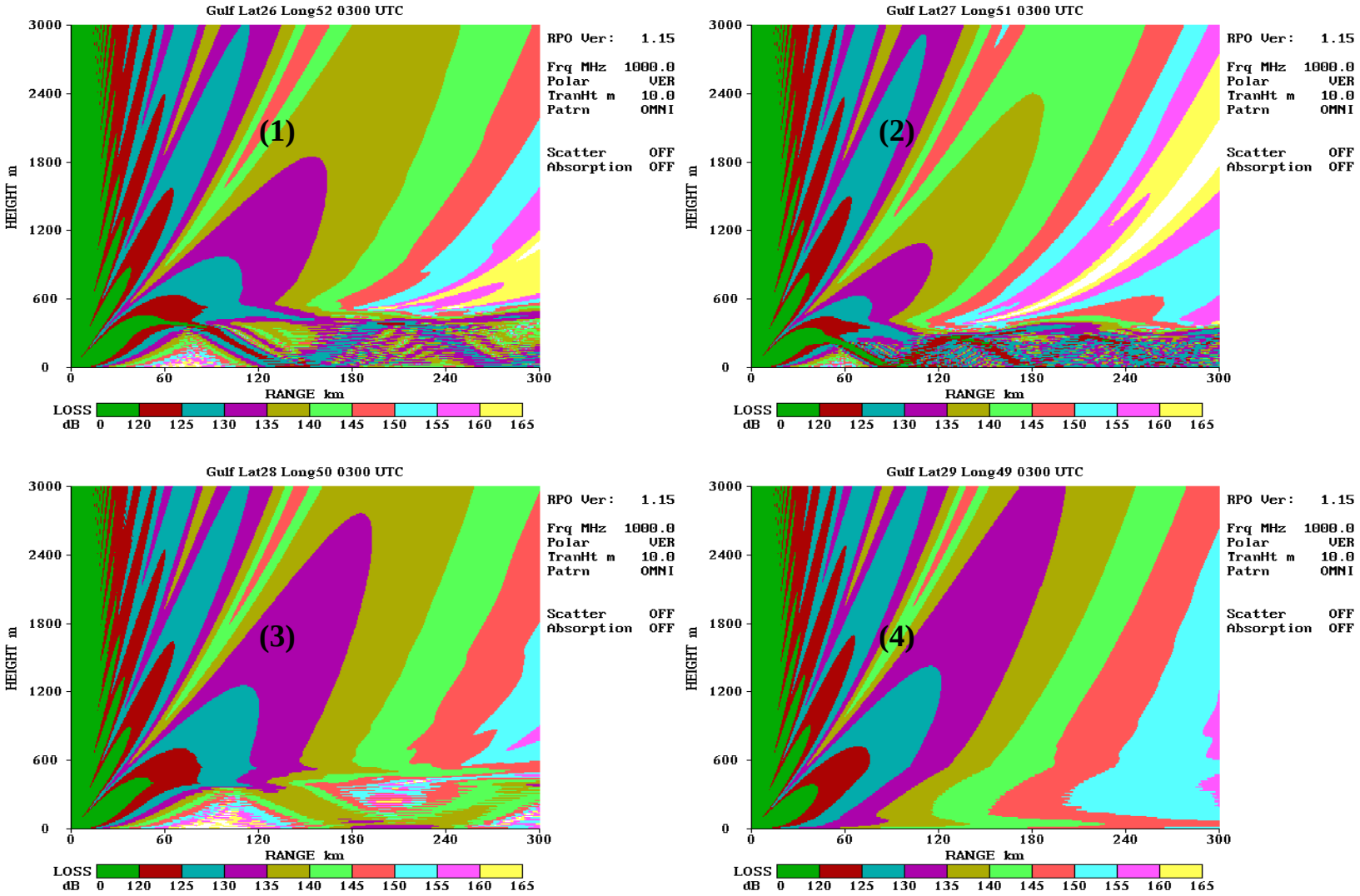


**Figure 4.16.** Radio propagation associated with profiles in Figure 4.15 where the numbers refer to locations in Figure 4.1.

Figure 4.17 shows data in a time frame six hours later than in Figure 4.15. This figure shows that the strongest area of ducting appears to be near 26° latitude and 52° longitude, with a peak-to-peak differential of about 70 M-units over a range of 100 meters in altitude. Moving northwest from this location, the duct intensity decreases dramatically. The next location shows a 50 M-unit differential, and the next shows 20, while the farthest location from 26° lat. and 52° long. shows no ducting conditions whatsoever. The propagation effects are shown in Figure 4.18. The first plot shows the strongest bending of radio waves, while the second plot exhibits this behavior in a slightly weaker fashion. Because the duct is small and elevated in the third plot, no ducting takes place, and in the last plot, typical attenuation of the wave is observed. Once again, it can be observed that the refractive conditions taking place occur on a fairly large regional scale.

Finally, Figure 4.19 shows the data from the same four locations at 15:00 UTC. All four locations show refractive conditions conducive to the ducting phenomenon. Water vapor decreases sharply with altitude, while once again a temperature inversion is noticed relatively close to the surface of the earth. The modified refractivity profiles, therefore, show very prominent surface-based elevated ducts. The fourth plot is unique in that the duct occurs very low to the ground, and so the sense that the main regional conditions relevant to ducting are centered somewhere around 26-27° latitude and 51-52° longitude. The RPO model in Figure 4.20 displays a very vivid picture of how radio waves would propagate given these conditions, and there is no difficulty in interpreting that a large amount of signal appears to traverse distances of more than 300 km, and further around the Earth's curvature.

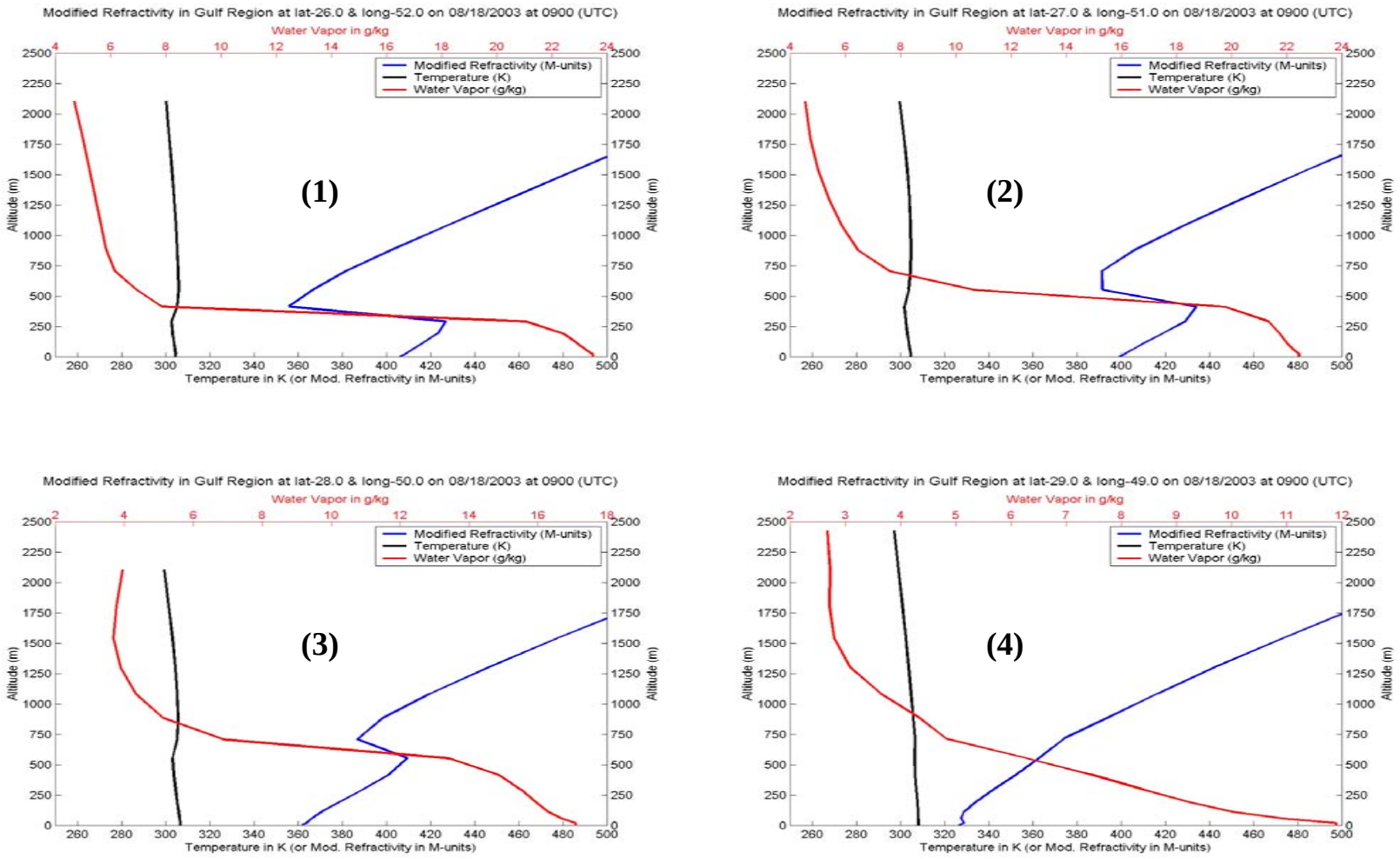


**Figure 4.17.** Gulf region profiles at 09:00 UTC show ducting in 3 out of 4 locations where the numbers refer to locations in Figure 4.1.

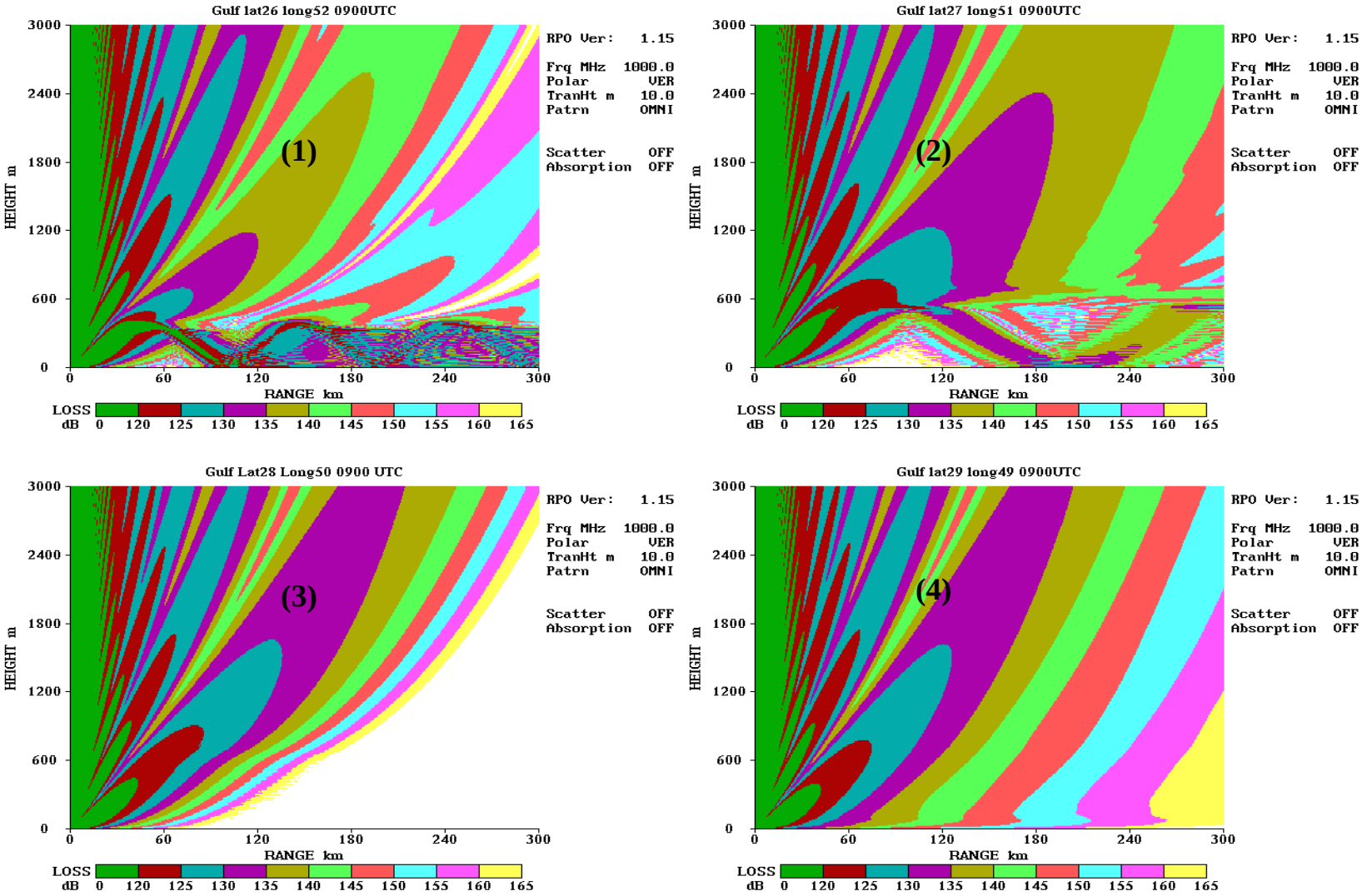


**Figure 4.18.** Radio propagation associated with profiles in Figure 4.17 where the numbers refer to locations in Figure 4.1.

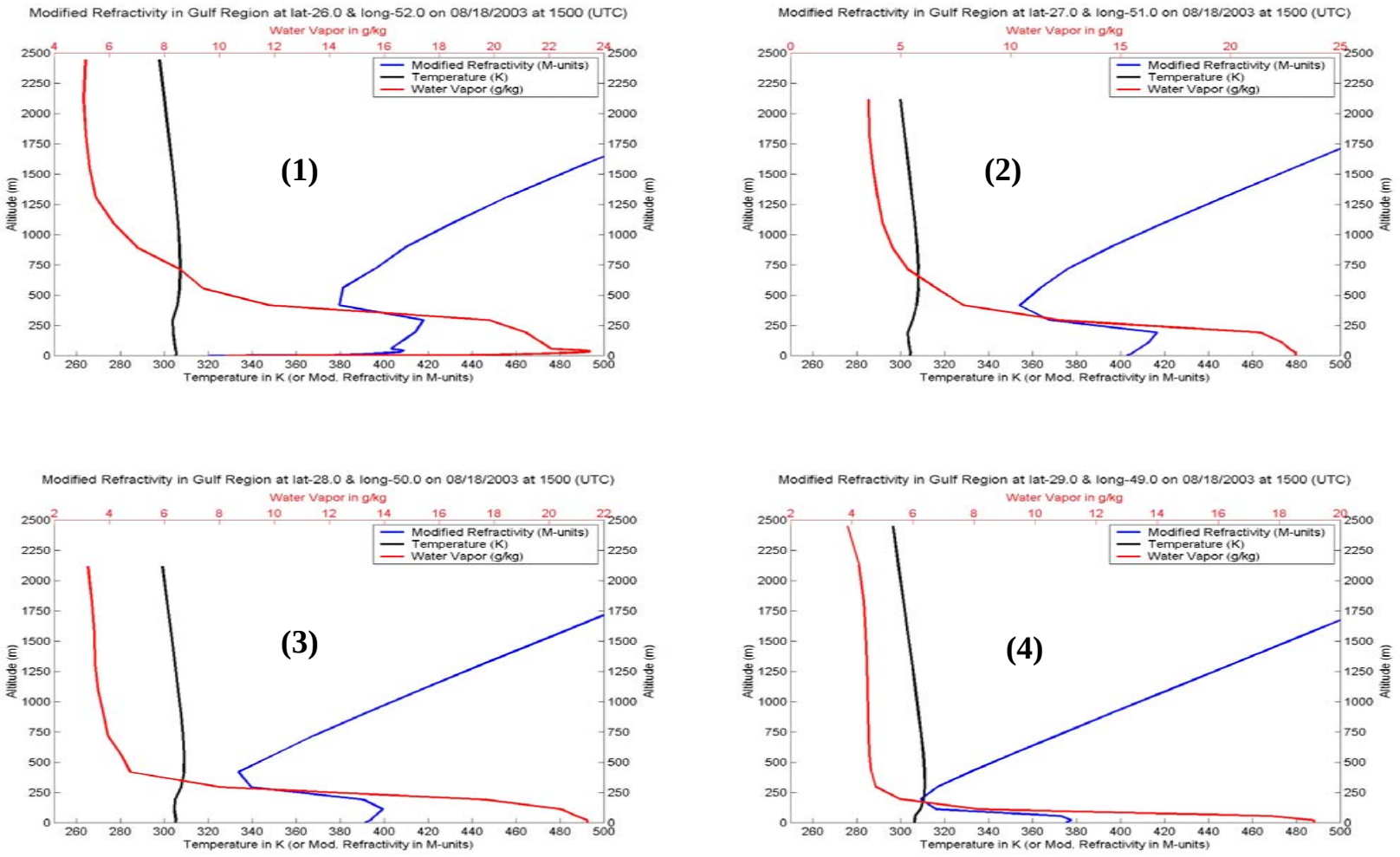


**Figure 4.19.** Gulf region profiles at 15:00 UTC show ducting in all 4 locations where the numbers refer to locations in Figure 4.1.

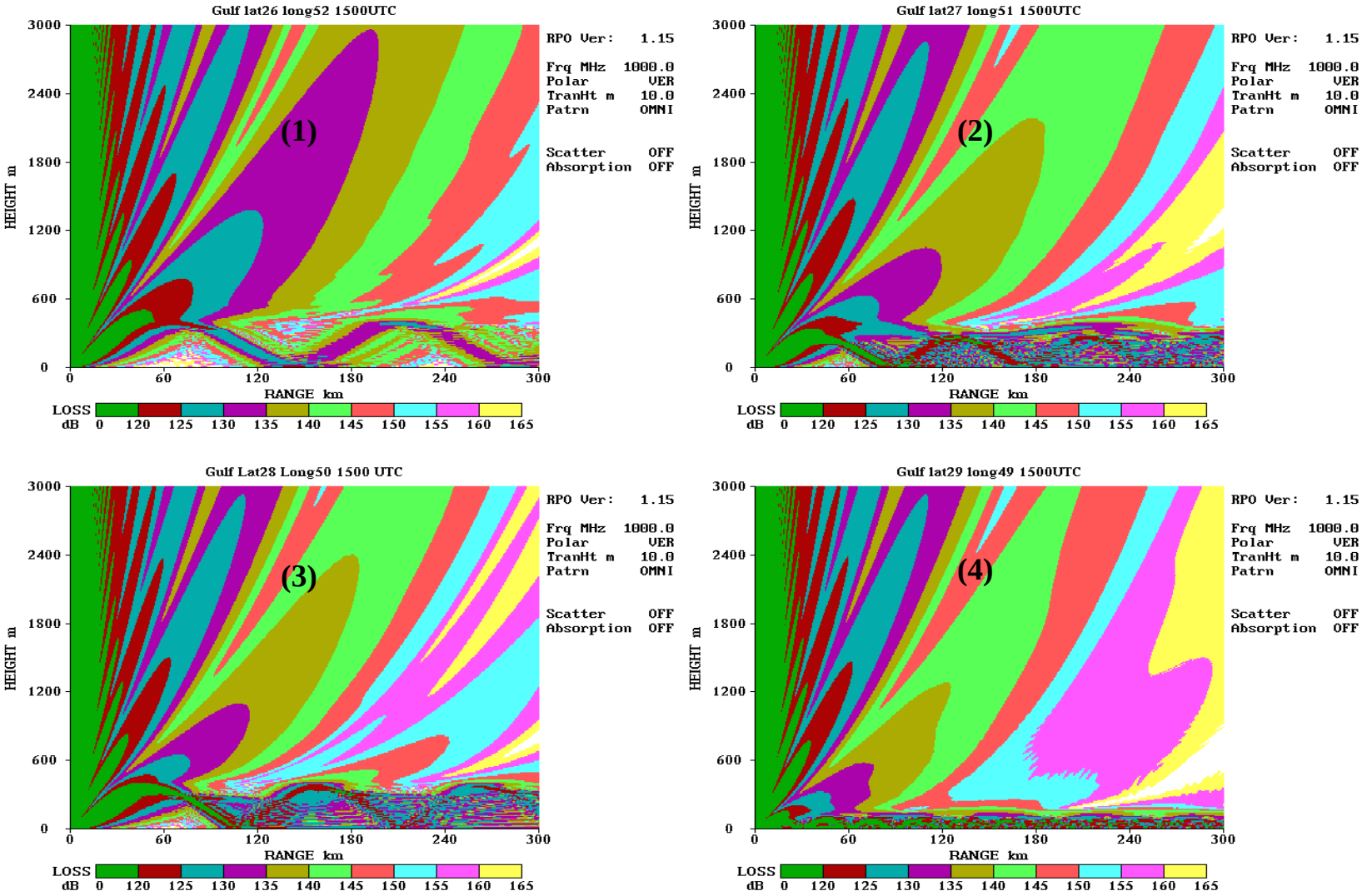


**Figure 4.20.** Radio propagation associated with profiles in Figure 4.19 where the numbers refer to locations in Figure 4.1.

Although Figures 4.15 through 4.20 seem to reinforce the notion that ducting events are regional rather than isolated, further investigation into this idea, as well as examination of temporal variation for a given location, is presented in Figures 4.21, 4.22, 4.23, and 4.24. The "virtual" time sequences displayed in these figures are created by adding multiples of 100 to the M-unit values for each 3-hour time period to allow enough spacing for analysis of the sequence. The absolute measurements are not as important in these graphs because the features of interest are the gradients rather than the values themselves.

A couple of interesting phenomena can be seen while examining the above-mentioned figures. The first is a spatial shift in the center of severe ducting conditions over time. In the first three time periods, including 0300, 0900, and 1200 UTC, locations 1 and 2 (corresponding to 26 Lat., 52 Long., and 27 Lat., 51 Long.) experience the most severe ducts, with the center likely located near location 1, as location 4 experiences no ducting, and location 3 exhibits one or two relatively weak ducts. However, during the hours of 1500, 1800, and 2100 UTC, it is without question that the most extreme ducting conditions exist at location 3 (corresponding to 28 Lat., 50 Long.) At location 2, the ducts pick up in intensity during this period, and location 4 ducts are seen for the first time. This indicates that the center of strongest ducting conditions has shifted closer to location 3.

The second feature of note involves temporal variation of refractivity at the same location. Location 1 has very little variability at all, as moderate ducting is present throughout the entire day on Aug. 18, 2003. Locations 2 and 3 exhibit moderate ducting at most times, but at both 0900 and 1200 UTC, the optimum coupling height of the ducts

increases by as much as 300 meters. In the case of location 3 at 0900 UTC, it has even been shown (in Figure 4.18) that this increase in duct height eliminates major radio wave

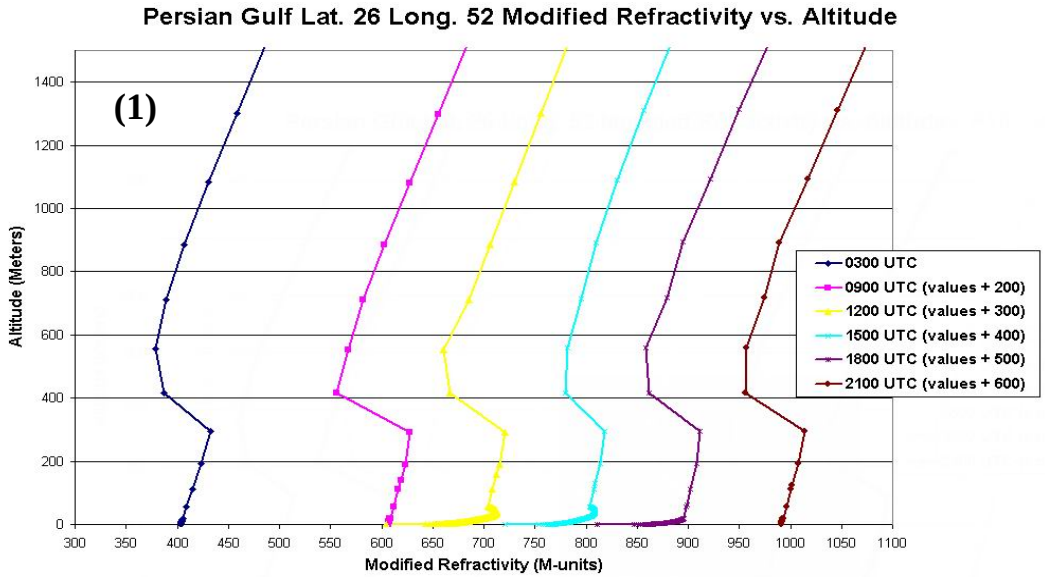


**Figure 4.21.** Gulf profiles for Aug. 18, 2003 (Lat. 26 Long. 52 – location (1) in Figure 4.1).

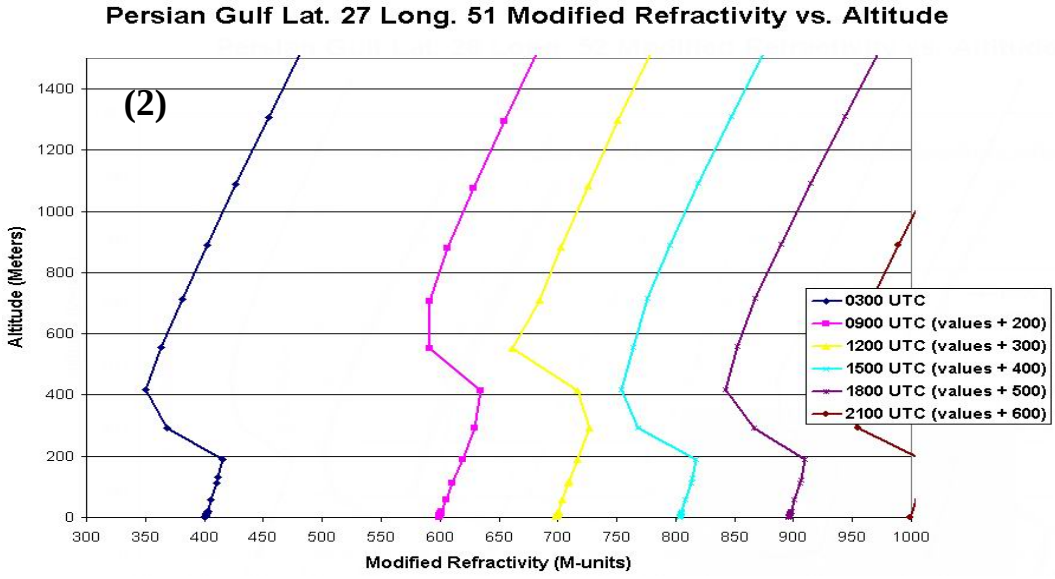


**Figure 4.22.** Gulf profiles for Aug. 18, 2003 (Lat. 27 Long. 51 – location (2) in Figure 4.1).

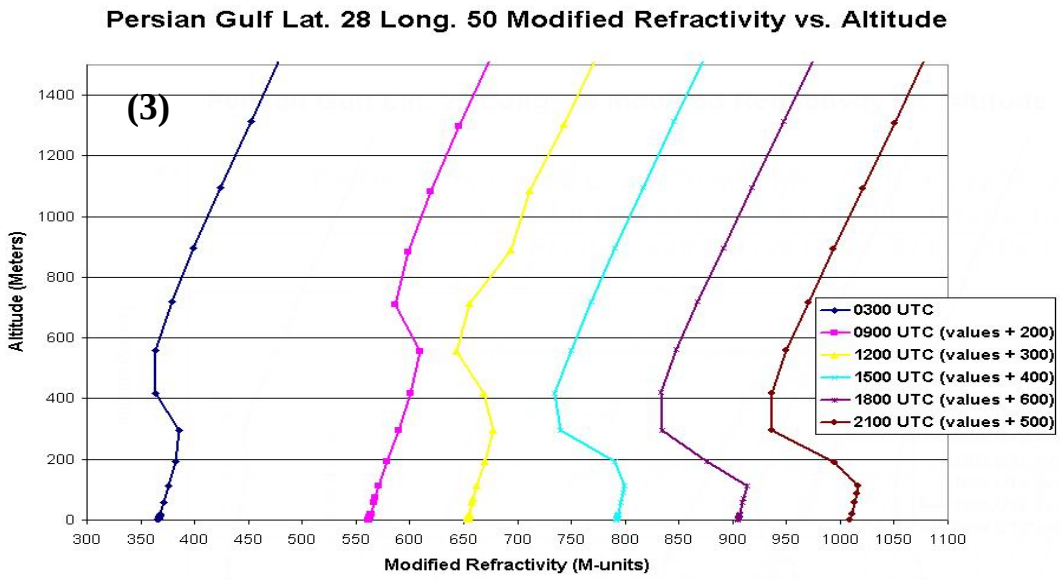


**Figure 4.23.** Gulf profiles for Aug. 18, 2003 (Lat. 28 Long. 50 – location (3) in Figure 4.1).

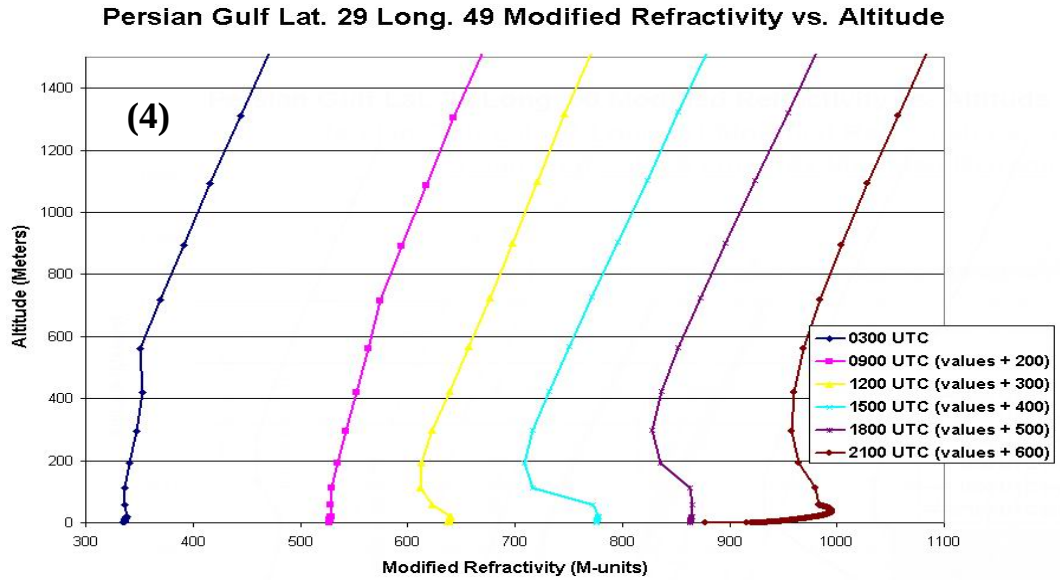


**Figure 4.24.** Gulf profiles for Aug. 18, 2003 (Lat. 29 Long. 49 – location (4) in Figure 4.1).

propagation problems. The increase in coupling height for locations 2 and 3 occurs at night locally, so it appears that locations 2 and 3 experience diurnal variation in duct height. Finally, location 4 shows the most inconsistent behavior. During the first three time periods, no ducts are present, but the last three all show conditions that represent the

formation of ducts. This behavior seems to vary diurnally as well, but generally this location does not seem to follow the behaviors of the other 3 locations. The reason for the erratic behavior may be because this location is the most distant from the center of where the regional ducting is most intense.

In the interpretation of the Persian Gulf data, the refractive conditions that cause ducting take place on a regional scale. In each time period presented, a definitive center exists that exhibits the strongest ducting phenomenon, followed by a decline as the more intense center location moves outward. It has also been shown that this "center of severity" shifts as a function of time. Because of these observations, a situation is imaginable in which a small number of lidar systems could be deployed on ships in a given region to fully describe the refractive conditions in the region. Instead of relying on weather forecasts for possible refractive information, the ships would be able to accurately determine the meteorological conditions, and then apply this knowledge to describe radio wave propagation characteristics in real time. This is a situation that is very much realizable, and could be considered a big step in improving the capability of our Navy's vessels.

# CHAPTER 5

# CONCLUSIONS

The capability of the Raman lidar to measure temperature and water vapor has been demonstrated and verified. Along with a surface pressure sensor, these allow profiles of RF refractivity to be calculated and thereby provide a determination of the way in which radio waves will propagate through the lower atmosphere. Because the conditions that lead to refractive effects appear to be regional, a very small number of Raman lidar systems mounted aboard Navy ships (two to five in a littoral area) would provide a useful operational display of how radio waves are propagating throughout that region.

A historical overview was given to provide insight as to how the RF refractivity problem has been handled in the past. A wide variety of instruments and techniques have been investigated and applied to better understand this phenomenon. An innovative method for visual inspection of lidar measurements of RF refractivity was developed during this investigation. Using the ratio, of the derived refractivity to the values calculated from the United States Standard Atmosphere, has proven to be valuable in quickly recognizing the probable times and locations where ducting conditions exist. This allows the pinpointing of interesting phenomenon within a given data set. A description of the Radio Physical Optics (RPO) model was given, and several output graphs were used to demonstrate the effects that refractive conditions have on radio wave propagation. Finally, measurements from two data sets have been examined, one using

the PSU LAPS lidar in the eastern U.S. coastal region, shown in Figure 4.2, and one in the Persian Gulf region, shown in Figure 4.1.

Measurements made by the Penn Sate LAPS lidar, aboard the US Sumner in September and October 1996, demonstrated the presence of elevated ducts, as well as one case of a surface duct. The refractivity ratio profile, which was presented for the first time in this thesis, assisted in finding interesting ducting conditions, and thus was able to show where further analysis was expected to yield a more useful understanding of the ducting phenomena. Overall, the PSU LAPS lidar has shown to be very capable in observing the variables that determine whether the conditions for ducting events exist.

Data from the Persian Gulf region were presented that showed cases of intense RF ducting. These data, provided by Remcom Inc., were obtained from the MM5 model that was used by the Air Force Weather Agency, and which described the meteorological environment of the region during August 2003. The results have shown that ducts with a differential of up to 70 M-units existed over a short altitude range, and that these ducts display a regional characteristic. Because the four locations of the obtained data were relatively close, a statement could be made on how much the refractive conditions varied over a regional scale. These locations were far enough apart to observe a center of strong ducting conditions, and the magnitude of these conditions decreased with distance from that center. The data also showed that this "center of severity" shifted with time. These observations paved the way for the understanding that three or four ship based lidars in a given region, of comparable size to that presented in this thesis, would be expected to provide an accurate real-time picture of refractive conditions in that region.

## REFERENCES

Balsiger, Franz, Paul T. Haris, and C. Russell Philbrick, “Lower Tropospheric Temperature Measurements Using a Rotational Raman Lidar,” Optical Instruments for Weater Forecasting, SPIE Vol. 2832, 53 – 60, 1996.

Chadha, Ginnipal S., “ Optical Systems Design for ALAPS Lidar Instrument,” Master of Science Thesis for Penn State University, Department of Electrical Engineering, May 2001.

Davidson, K.L., C.H. Wash, "Remote Measurement of Atmospheric Refraction Conditions in the Coastal Region," AGARD Conference Proceedings 567, Propagation Assessment in Coastal Environments, Feb. 1995.

Dockery, G. Daniel, "Modeling Electromagnetic Wave Propagation in the Troposphere Using the Parabolic Equation," IEEE Transactions on Antennas and Propagation Vol. 36 No. 10, 1464 - 1470, Oct. 1988.

Dockery, G. Daniel, Julius Goldhirsh, "Atmospheric Data Resolution Requirements for Propagation Assessment: Case Studies of Range-dependent Coastal Environments," AGARD Conference Proceedings 567, Propagation Assessment in Coastal Environments, Feb. 1995.

Esposito, Steven T., “Applications and Analysis of Raman Lidar Techniques for Measurements of Ozone and Water Vapor in the Troposphere,” Master of Science Thesis for Penn State University, Department of Electrical Engineering, May 1999.

Kerr, Donald E., Propagation of Short Radio Waves. Peninsula Publishing, 1988.

Haris, P. T., “Pure Rotational Raman Lidar for Temperature Measurements in the Lower Troposphere,” Ph.D. Dissertation, The Pennsylvania State University, 1995.

Helvey, R., J. Rosenthal, C.R. Philbrick, T.J. Kane, and D.B. Lysak, Jr., "Lidar and Radiosonde Measurements of Coastal Atmospheric Refraction," Atmospheric Propagation and Remote Sensing III, SPIE Vol. 2222, 288-298, 1994.

Hitney, Herbert V., "Hybrid Ray Optics and Parabolic Equation Methods for Radar Propagation Modeling," Radar 92. International Conference, 58 - 61, Oct., 1992.

Hitney, Herbert V., Radio Physical Optics (RPO) Program Version 1.15 User's Guide, Naval Command, Control and Ocean Surveillance Center, Aug. 1995.

Lowry, Anthony R., Chris Rocken, Sergey V. Sokolovskiy, and Kenneth D. Anderson, "Vertical Profiling of Atmospheric Refractivity from Ground-based GPS," Radio Science, Vol. 37, No. 3, 2002.

Measures, Raymond M., Laser Remote Sensing.Wiley-Interscience, New York, 1984.

Mulik, Karoline R., "Evolution of Ozone and Particulate Matter During Pollution Events Using Raman Lidar," Master of Science Thesis for Penn State University, Department of Electrical Engineering, May, 2000.

Nave, C.R., Department of Physics and Astronomy, Georgia State Univeristy, http://hyperphysics.phy-astr.gsu.edu/hbase/electric/diph2o.html#c2, 2003.

Patterson, W.L., Integrated Refractive Effects Prediction System (IREPS) User's Manual, Revision PC-2.0, Technical Document 1874, Naval Ocean Systems Center, August, 1990.

Paulus, Richard A., "An Overview of an Intensive Observation Period on Variability of Coastal Atmospheric Refractivity," AGARD Conference Proceedings 567, Propagation Assessment in Coastal Environments, Feb. 1995.

Philbrick, C.R., "Raman Lidar Measurements of Atmospheric Properties," Atmospheric Propagation and Remote Sensing III, SPIE Vol. 2222, 922-931, 1994.

Philbrick, C.R., "Overview of Raman Lidar Techniques of for Air Pollution Measurements," Lidar Remote Sensing for Industry and Environment Monitoring II, SPIE Vol. 4484, 136 - 150, 2001.

Philbrick, C.R., "Application of Raman Lidar Advancements in Meteorology and Air Quality Monitoring," Lidar Remote Sensing for Industry and Environment Monitoring III, SPIE Vol. 4893, 61 - 69, 2002.

Philbrick, C.R., and D.W. Blood, "Lidar Measurements of Refractive Propagation Effects," AGARD Conference Proceedings 567, Propagation Assessment in Coastal Environments, Feb. 1995.

Remcom, Inc. "Software Requirements Specification for the Electromagnetic Propagation Integrated Resource Environment," June, 2003.

Salby, Murry L., Fundamentals of Atmospheric Physics. Academic Press, San Diego, CA, 1996.

Slick, C.T., "Lower Tropospheric Temperature Measurement Scheme for an Advanced Lidar Atmospheric Profiling System," Master of Science Thesis for Penn State University, Department of Electrical Engineering, May, 2002.

Stull, R. B., An Introduction to Boundary Layer Meteorology, Kluwer Academic Publishers, Dordrecht, The Netherlands, 1997.

U.S. Standard Atmosphere, Washington, D.C., October 1976.

Verghese, Sachin J., "Characterization of Low-Level Jets and their Influence on Air Pollution Using Raman Lidar and Wind Profiling Radar/RASS," Master of Science Thesis for Penn State University, Department of Electrical Engineering, August, 2003.

Wave Propagation Panel, "Radio Wave Propagation Modeling, Prediction and Assessment," NATO AGARD Monograph AG-326, Ed. J. H. Richter, 1990.